Ecohydrology

WILEY

RESEARCH ARTICLE OPEN ACCESS

Monitoring and Modelling Fluxes of Water and Nutrients to Surface Drainage Network From Irrigated Agricultural Fields in a Hydraulically Reclaimed Coastal Area

Antonio Coppola[1,2] | Raffaella Zucaro[3] | Silvia Baralla[3] | Marco Satta[3] | Myriam Ruberto[3] | Alessandro Comegna[1] | Giovanna Dragonetti[4] | Shawkat Basel Mostafa Hassan[1]

[1]School of Agricultural, Forestry, Food and Environmental Sciences (SAFE), University of Basilicata, Potenza, Italy | [2]Dept. of Chemical and Geological Sciences (DCGS), University of Cagliari, Cagliari, Italy | [3]Research Centre for Agricultural Policies and Bioeconomy, Council for Agricultural Research and Economics (CREA), Rome, Italy | [4]Sustainable Water & Land Managament in Agricultural Ecosystems Division (W&L), Mediterranean Agronomic Institute of Bari (CIHEAM Bari), Bari, Italy

Correspondence: Shawkat Basel Mostafa Hassan (shawkat.hassan@unibas.it)

Received: 13 November 2023 | **Revised:** 2 September 2024 | **Accepted:** 5 September 2024

Funding: This work was supported by Programma Operativo Nazionale R&I.

Keywords: agrohydrological modelling | kinematic wave theory | nutrient transport | soil water and solute monitoring

ABSTRACT

This paper describes the application of a physically based agrohydrological model (named FLOWS), coupled with a kinematic wave approach model (named KWV) for water and solute runoff routing, for interpreting the fate of water and nutrients coming from cultivated fields to surface drainage network located in 'Piana del Sassu' in the Arborea plain, a hydraulically reclaimed area with shallow groundwater. Modelling was supported by a large complex database on soil, groundwater and surface drainage water, which was used for establishing the boundary conditions for simulations, as well as for calibrating and validating the model. The model FLOWS provided the water and nutrient fluxes to the surface water, which were passed to the KWV model for their routing along the elementary fields in the experimental area and from these to the ditches and finally to the drainage channel. The modelling approach effectively predicted the water and solute distribution along the soil profile, as well as the losses of water and nutrients to the surface water. The results showed a significant amount of water and dissolved nutrients to flow quickly from the soil uppermost layer to the surface drainage network during both the irrigation season and during rainfall events. During irrigation applications, losses were mostly due to rainfall intensity exceeding the maximum infiltration velocity of the shallow soil layer in the case of sprinkler irrigation and to subsurface lateral drainage in the case of exceeding irrigation water provided by drip irrigation. This makes the Sassu plain a significant contributor of nutrients (nitrate and phosphorus) to the surface water. Consequently, even though the agricultural activities might not be an important issue for the groundwater vulnerability, the management of water and nutrients should be significantly improved to avoid ecohydrological threats to the important coastal water bodies present in the area.

1 | Introduction

Chemical pollution of soils, surface water and groundwater is frequently the consequence of human activities, among which agriculture is undoubtedly one of the most important. The use of fertilizers and other agrochemicals makes the agricultural sector one of the main sources of diffuse pollution for soil and water resources. Of particular importance is the pollution of aquifers and surface water by nutrients (mostly nitrogen and phosphorus). Many areas of intensive agriculture and livestock activity

are affected by nonpoint source (NPS) pollution of aquifers and surface waters (estuaries, lakes, wetlands, etc.). The inputs of livestock manure, together with the inputs of synthetic fertilizers, can often generate surpluses of N in the soil. The nitric fraction of this nitrogen, which is naturally formed in the more superficial horizons of the soil in aerobic conditions, can either percolate below the soil thickness explored by the roots or it can reach the surface water network through artificial drainage network and/or surface runoff, in the case of rainfall and/or inefficient irrigation management. The excess nitrogen that remains in the soil profile at the end of the crop's vegetative cycle, when the nitrification processes are still active and root uptake of nitrate is null, is then easily transported towards the water table or to the surface drainage network by the precipitation.

In Europe, in the perspective of reducing pollution of water bodies, a set of rules and regulatory mechanisms have been set out in national and supranational regulations that farmers have to comply with to preserve the environment and meet the recent new Green Deal strategy. In 1991, the European Union adopted the Nitrates Directive (91/676/CEE) to protect water quality by preventing nitrate leaching from agricultural activities and promoting the adoption of Good Agricultural Practices (GAP). The directive imposed the identification of nitrate vulnerable zones (NVZs), where farmers are required to comply with specific limits of inorganic fertilizers and organic slurry application rates (not more than 170 kg/ha/year of N). The regulatory and mandatory (even through sanctions) approach has not been fully successful. In most of the NVZs, nitrate concentration in water bodies frequently still exceeds the limit of 50 mg/L of NO_3 (11.6 mg/L of N-NO_3) allowed for drinking water. Likewise, many surface water bodies still suffer from periodical algal blooms and murky waters, which poses serious conflicts between aquatic ecosystems and agriculture. The European Community report (European Commission 2021), describing the progress towards the objectives set by the Nitrates Directive for the period 2016–2019, concluded that for both groundwater and surface waters, a considerable part of the Member States still faces significant challenges in achieving the objectives of the Nitrates Directive regarding nitrate in groundwater and eutrophication of surface waters. For example, for surface waters, as an average in the Member States, 36% of the rivers, 32% of the lakes, 31% of the coastal waters, 32% of the transitional waters and 81% of marine waters were reported as eutrophic (European Commission 2021).

This is the case of the Arborea area (Sardinia Region, Italy), which is a hydraulic reclaimed area and also one of the main NVZs identified by the Sardinia Region, as the application of animal manure to the fields, as well as mineral nitrogen fertilizers, generates high nutrient loads to the shallow groundwater and the surface artificial water drainage network, draining to some important ponds and wetlands located along the coast line. In the area, despite some improvements after the first year of NVZ restrictions, many wells still register values even far above the limit of 50 mg/L (Ghiglieri et al. 2016), and wetlands are periodically subjected to eutrophication and fishery issues (Nguyen, Seddaiu, and Roggero 2014).

The partial failure in the regulatory approach may be ascribed, at least partly, to technical–physical reasons. Specifically, the problem arises from two main reasons: (1) inadequate agronomic management of fertilizers, which leads to a low efficiency of nutrient use by crops, and (2) inefficient irrigation management, inducing losses of water and dissolved nutrients as deep percolation fluxes and/or runoff fluxes. This may not be necessarily ascribed to farmers. Actually, the GAP themselves, even when the farmer wants actually to apply them, are not site specific and may produce very different—sometimes even worsening—results depending on the site-specific physical conditions (soil hydrological regime, climate, ecological conditions hindering natural denitrification, etc.). This means that, for given environmental conditions, minimizing nutrient losses to water bodies may require more site-specific agronomic practices, in terms of irrigation water and fertilizer management, for example. This cannot prescind from a better understanding of the physical–hydrological behaviour of the soil-vegetation system under management and its hydrological interactions with ground and surface water bodies. In this direction, combining adequate soil monitoring methodologies to numerical agrohydrological models provides a powerful opportunity to identifying the fundamental interacting process mechanisms controlling water dynamics and nutrient transformations and transport through the unsaturated zone and from this to the groundwater, as well as water and solute fluxes to the surface water through runoff and drainage, under given environmental and soil agronomic management practices.

Monitoring tools are now available for improved physical and geochemical characterization of the vadose zone at very different scales, including non-invasive geophysical methods (Coppola et al. 2016). These tools may provide the information on the prevailing top- and bottom-boundary conditions to be used to run the models, as well as the data for their calibration and validation. When adequately supported by data, these models may us allow to reliably identify the best site-specific water and nutrient management and to prevent NPS pollution of water bodies, by providing more informed decisions on irrigation water and nutrient application, better tailored to crop needs, as well as to their ecohydrological impact (Hassan et al. 2022, 2023). Of course, for their reliable application, these models cannot disregard the real behaviour of the farmers in managing irrigation water and fertilizers, the irrigations systems, the agronomic techniques adopted, which have all to be accurately identified before any model application.

With these premises, this paper describes the application of a physically based agrohydrological model, coupled to a kinematic wave approach for runoff routing, for interpreting the fate of water and nutrients coming from cultivated fields to groundwater and surface drainage network located in the Arborea area, specifically in the so-called Piana del Sassu area. Even if characterized by a very shallow water table, the Piana del Sassu area is not included in the NVZ because of the low hydraulic conductivity of the soils. And, yet, a significant amount of water and dissolved nutrients is expected to flow quickly from the uppermost layer of the soil to the surface drainage network in the case of rainfall events, as well as during the irrigation season, when the rainfall intensity of the sprinkler systems frequently exceeds the maximum infiltration velocity of the shallow soil layer. This may happen by either direct surface runoff or subsurface drainage flow. To

us, verifying and understanding these transport mechanisms are crucial for the management of agricultural activities in the Piana del Sassu soils, which in this case contribute significant amounts of nutrients (nitrate and phosphorus) to the S'Ena Arrubia wetland, even though the area does not formally fall within the Arborea NVZ and thus it is not subject to the limit of 170 kg/ha of N fertilizer supplies imposed to the NVZs. Identifying and describing these pollution mechanisms are exactly the issue dealt within this paper.

Modelling was supported by a large database on soil, groundwater and surface drainage water, which was used for establishing the boundary conditions for simulations, as well as for calibration and validation of the model. The final aim was understanding the main physical mechanisms inducing the losses of water and nutrients to both groundwater and surface water bodies, with a view, on one side, of optimizing the irrigation water and fertilizer management and, on the other side, of quantifying the water and nutrient fluxes to be eventually treated by denitrification technologies such as bioreactors and artificial wetlands, which have to be developed in the area for preventing pollution of water before it is returned to groundwater and the surface drainage network.

2 | Materials and Methods

2.1 | Study Site

The study site is located in the so-called Piana del Sassu (UTM coordinates: 4406931.86 m N, 470343.77 m E) as shown in Figure 1. It is part of the Arborea territory (Sardinia Region, Italy), which is a hydraulic reclamation area characterized by intensive livestock activities. Thus, most of the land is cultivated with corn and alfalfa crops, from which the farmers obtain part of the feed for cattle.

The Arborea territory represents a quite complex ecohydrological system. It is delimited by and interacts with a system of lagoons and coastal ponds, relevant from an environmental point of view for the richness of fauna and flora. Most of them are classified as Sites of Community Importance (SCI) under the Natura 2000 network and are specifically regulated as a Special Area of Conservation (SAC) under the Habitats Directive.

As for groundwater, the area of Arborea falls entirely within the Plio-Quaternary detritic alluvial aquifer of Campidano. In the superficial sandy level, there is a phreatic aquifer with a freely fluctuating water table used in the past for domestic use through large-diameter wells with an average depth of 4 m. These shallow wells have very limited flow rates and dry up if subjected to pumping for a few hours. The depth to the water table varies between about 1 and 5 m. The trend of the piezometric surface indicates a water flow directed mainly towards the coast and partly towards the interior of the area to the Piana del Sassu. Below the shallow phreatic aquifer, there are several aquifers, mostly sandy–pebbly, separated by low–hydraulic conductivity clay layers.

The Arborea hydraulic reclamation area includes two distinct subareas: (1) the Piana di Arborea, made up of sandy deposits, and (2) the Piana del Sassu, made up of silty and clayey deposits. The geomorphological and pedological characteristics reflect the different origins of the two areas, which involved distinct reclamation interventions.

The reclamation of the Piana di Arborea mainly consisted of the flattening of the dune formations and the filling of the humid depressions. Locally, in relation to the low water table depth of the surface aquifer and humid depressions, relatively deep drainage channels were created to intercept the aquifer and drain the land. The elementary agricultural unit of this part of the Arborea reclamation area is a field of about 4 ha (400 m × 100 m) often delimited by a longitudinal ditch. Due to the very high soil infiltration capacity and the very low depth to the water table, the NO_3 concentrations in many wells of the area are well above the limit of 50 mg/L. Accordingly, the area is one of the most important NVZs identified by the Sardinia Region.

By contrast, in the Piana del Sassu, where the study site is located, soil profiles are generally characterized by the presence of very low–hydraulic conductivity surface layers, whose thickness may sometimes even be of 70–100 cm. However, if we look at the whole soil profile, there may be a significant variability, so that, in some areas, soil profiles are entirely of clayey texture whereas in other cases, the thick clay surface layer lies above very conductive sandy layers. In the Sassu area, the reclamation interventions simply consisted of a superficial arrangement of soil, by inducing some surface convexity aimed at rapidly removing the water runoff forming on the soil after rainfall events and excess irrigation and conveying it towards a dense network of drains and canals, and from these to the wetland of S'Ena Arrubia (which is both an SCI and an SAC). The elementary agricultural units consist of a field measuring approximately 0.5 ha (200 m × 25 m), which is drained by a longitudinal ditch flowing to a main drainage channel. Due to the low infiltration capacity of the shallow soil layer, the area is not included in the Arborea NVZ, as the aquifer is considered quite protected by vertical percolation flows. Due to the profile variability, however, this may be true for some soils but has to be verified for soil profiles with high-conductivity sandy layers. For sure, in the area, significant nutrient concentrations are frequently observed in the surface drainage network draining the area, which are supposed to come from the uppermost layer of the soil in the case of rainfall events, as well as during the irrigation season, as sprinkler systems used for irrigation provides rainfall intensity frequently exceeding the maximum infiltration velocity of the shallow soil layer.

2.2 | The Experimental Field and the Monitoring System

The experimental field, of about 16 ha, was selected based on the hydropedological characteristics of the soils found in the area and on the physical–morphological characteristics of the entire soil–groundwater–surface network system. As for the latter point, the selected field represents a sort of field-scale model for the entire Sassu area, as it is a quasiclosed system where the field drains in a well-identified drainage network whose fluxes can be traced back mostly to the field itself. Figure 1 shows the location and a schematic view of

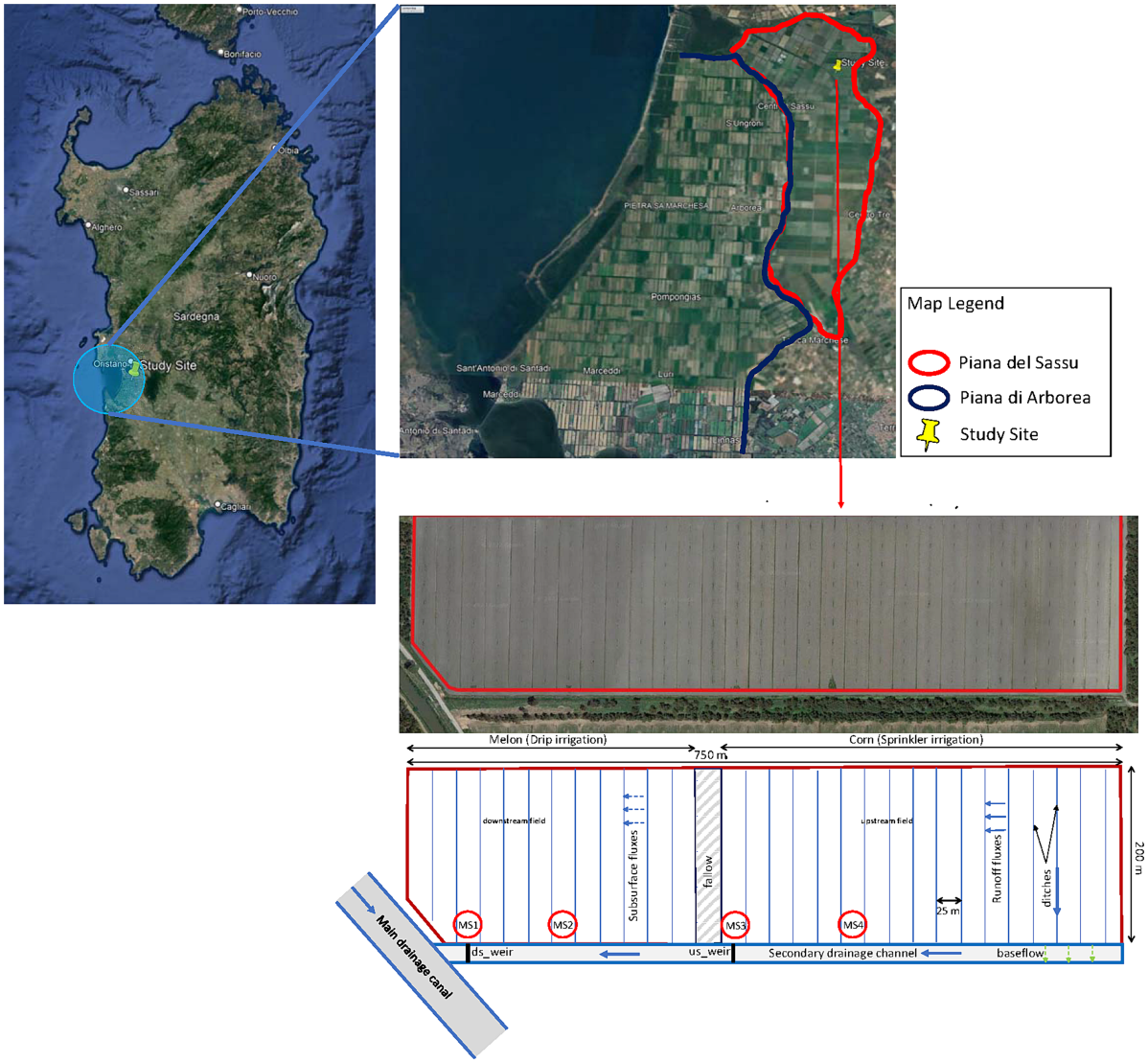

FIGURE 1 | On the top left, a map of the location of the study site in Sardinia Island; on the top right, a map showing the 'Piana di Arborea' in blue border and the 'Piana del Sassu' in red border; and to at the bottom right, a schematic view (not to scale) of the whole experimental field and its upstream (UsF) and downstream (DsF) subfields considered for analysing the experimental data. MS = monitoring station; ds_weir = downstream weir; us_weir = upstream weir. The green arrows represent the direct contribution of the shallow groundwater to the water and solute fluxes in the secondary drainage channel. The crop pattern refers to 2021. In 2022, both subfields were cultivated with corn. The physical–hydrological characteristics of the soils in the four MSs are given later in Table 1.

the experimental field, along with the spatial pattern of soils found within the field. Based on the soil distribution, the field was divided in two subfields, respectively named upstream field (*UsF*) and downstream field (*DsF*).

Being a reclamation area, the whole field is divided into smaller strips of approximately 0.5 ha in size, 25 m wide and 200 m long. The fields are drained through 200-m-long ditches, with an approximately rectangular cross section about 60 cm deep and 60 cm wide, arranged along the longitudinal dimension of the field. The drains flow into a secondary drainage channel approximately 750 m long (with a trapezoidal cross section 1.5-m depth, top width 6 m and bottom width 2 m) which, in turn, flows into a main canal called 'Canale delle Acque Basse', which conveys the drainage waters of the entire area towards the final receiving water body (S'Ena Arrubia Pond).

In 2021, the experimental field was cultivated with melon (the DsF), irrigated by drip irrigation, and with corn (the UsF), irrigated by sprinkler irrigation. In 2022, both the subfields were cultivated with corn and irrigated by sprinkler irrigation.

The drip irrigation system consisted of dripper lines, with 2-L/h drippers at a distance of 30 cm along the line and 0.8 m between lines. Due to the low conductivity of the soil and the irrigation volumes provided at each irrigation, the wetted area during the irrigation almost closed the flow field, thus inducing a quasi-1D flow immediately below the soil surface.

The sprinkler irrigation system consisted of nine sprinklers with an irrigation range of 20 m and a flow rate of 1 L/s at a pressure of 2 bars.

In each of the subfields, two automatic monitoring stations (MSs) were installed equipped with (see Figure 1) CS655 water content reflectometer sensors (WCRs), tensiometers, multiparametric probes and water-level sensors. In each site, 12-cm-long CS655 WCR probes (Campbell Scientific, Inc.) were installed horizontally at five different depths ($z = 10$, 30, 50, 70, 90 cm), after digging a pit (see Figure 2).

The probes provide estimation of soil water content, θ; bulk electrical conductivity, EC; and temperature, T. As for the water content, the probe, which is a reflectometer, measures the number of reflected voltage pulses per second, *fr*. The true output of the probes is a period, *P*, which is inversely related to *fr*. The period is divided by a dimensionless scaling factor, *Sc*, to facilitate recording by a datalogger, giving the propagation time, t_{pr}, for the reflectometer (Kelleners, Paige, and Gray 2009).

EC is estimated by CS655 probes by exciting the waveguides with a known nonpolarizing wave and measuring the signal attenuation due to free ions in soil solution, providing electrical conduction paths that result in attenuation of the signal applied to the waveguides.

Signal attenuation is expressed as a voltage ratio, VR, which is quadratically proportional to EC. The measured signal attenuation is also used to correct for the loss effect on reflected voltage detection and thus propagation time, t_{pr}, estimation. According to the technical specifications provided by Campbell scientific, this loss effect correction allows accurate water content

FIGURE 2 | Pictures of one of the four MSs. (a) Overview of the station. The pipe in red close to the station is a piezometer; (b) TDR probes and tensiometers installed at different depths along the soil profile; (c) triangular weir for measuring the flow rate by measuring the head of water upstream with a diver-type sensor. A multiparameter probe is installed near each of the two weirs.

measurements in soils with a bulk EC of ≤ 8 dSm^{-1} without performing a soil-specific calibration. The same specifications provide a range for σ_b from 0 to 8 dSm^{-1}.

The probe firmware internally converts the P and VR values to the apparent dielectric permittivity, ε_a, and bulk electrical conductivity, EC, by empirical calibration equations built by immersing sensors in solutions of varying permittivity and varying electrical conductivity at constant temperature. The ε_a, in turn, is converted to a water content by using the universal calibration equation provided by Topp, Davis, and Annan (1980).

Each MS was also equipped with two Jet-Fill–type tensiometers, 90 and 120 cm long, providing readings of soil water pressure head in the range between −100 and 0 kPa through a resistive bridge pressure transducer. The two tensiometers were installed at 80 and 110 cm, respectively. The tensiometers were used to measure the hydraulic gradient and from this, knowing the hydraulic conductivity, the water flows in correspondence with the control plane at 90 cm. As will be clarified later in the section on modelling, the average pressure head measured at the two depths was used as variable pressure head bottom-boundary conditions for the simulations.

All the four MS were also equipped with a multiparameter probe with a diameter of 42 mm for the measurement of the following parameters: dissolved oxygen, DO (via optical sensor); electrical conductivity, σ_b; pH; redox potential, ORP; total dissolved solids, TDS; temperature; and water level. Furthermore, the probe allows the measurement of the nitrate concentration by means of an ion-selective electrode for nitrate ion. The multiparameter probes were installed either in the secondary drainage channel (at MS1 and MS3) or in the piezometers (at MS2 and MS4).

In detail, the multiparametric probes of MS1 and MS3 were immersed at a known depth, through access and inspection pipes, in the secondary drainage channel, each close to a triangular steel weir (with an angle of 120°) specifically installed to measure water discharge coming from the experimental field. A weir was installed in the downstream section of the canal, near the outlet of the secondary drainage channel, and allowed to measure the total volumes drained from the entire field. The second weir was installed further upstream, between the two subfields. During 2021, the two weirs allowed distinguishing the volumes returned to the surface drainage network from each of the two crops. Flow measurement with weirs was carried out by measuring the head of water immediately upstream of the weir. For this purpose, a Baro-Diver level sensor (van Essen Instruments), with a measurement range of 150 cm, was installed through access and inspection pipes, along with a barometric compensator.

The multiparametric probes of MS2 and MS4 were each immersed in a piezometer, installed close to the MS2 and MS4. The piezometers were installed at a depth of about 5 m from the soil surface. The piezometers consisted of a 3-in. PVC pipe with bottom and surface plugs and with the filter extending from 1.5- to 5.0-m depth from the ground surface. The installation was completed by filling the interspace between the soil and piezometer wall with calibrated gravel in the filter part and insulating the blind part with a bentonite layer of suitable thickness. Finally, the piezometers were purged until the water was clarified with a low-pressure compressor and ejector. The piezometer inlet was equipped with an inspection well sealed at the base with a cement mixture.

All the sensors were acquired by a datalogger with an SDI-12 interface (Serial Digital Interface at 1200 baud), which could be queried via a datalogger support software and which simultaneously sent data to the database management platform via FTP protocol.

Beside measuring nitrates by the ion-selective electrode for nitrate, periodic measurements of phosphorus were carried out in the secondary drainage channel by collecting water samples in correspondence to both the *us_weir* and *ds_weir* and analysing the phosphorus concentration by a photometric method carried out by a filter photometer AL450 AQUALYTIC and using the molybdenum blue reaction using ascorbic acid. With this method, the orthophosphate ion ($PO4^{3-}$) reacts with ammonium molybdate and antimony potassium tartrate under acidic conditions to form a complex. This complex is reduced with ascorbic acid to form a blue complex that absorbs light at 880 nm. The absorbance is proportional to the concentration of orthophosphate in the sample.

2.3 | The Models

For the purposes of this study, the modelling tools have to enable the simulation of all the water and dissolved nutrient balance components, including the fluxes of water and solutes from the soil to the runoff and to the subsurface drainage induced by excess water. Once these fluxes have been quantified, they must be routed to the surface drainage network in the case of rainfall events, as well as during the irrigation season, when the rainfall intensity of the sprinkler systems frequently exceeds the maximum infiltration velocity of the shallow soil layer. As mentioned, these processes are largely expected in the study area soils, where, due to the physical–hydrological properties of soils, a significant amount of nutrients (nitrate and phosphorus) are expected to reach the surface water bodies by runoff and lateral flow at the interface between tilled and untilled soil layers.

Accordingly, in this study, an agrohydrological model named FLOWS (FLOw of Water and Solutes in agri-environmental systems) was used to predict the water and solute fluxes to runoff and drainage eventually resulting from a single rainfall event and/or an irrigation application. Thus, a routing model based on the kinematic wave theory, named KWV, allowed routing of the water runoff water and dissolved solutes as overland flow and thus through the ditches and from these to secondary drainage channel and thus to the field outlet (see Figure 1). Figure 3 provides a schematic representation of the FLOWS–KWV coupling.

2.3.1 | The Agrohydrological Model

FLOWS is a physically based numerical model to simulate water flow and solute transport in agroenvironmental systems (Coppola et al. 2019a, 2019b; Hassan et al. 2023), allowing,

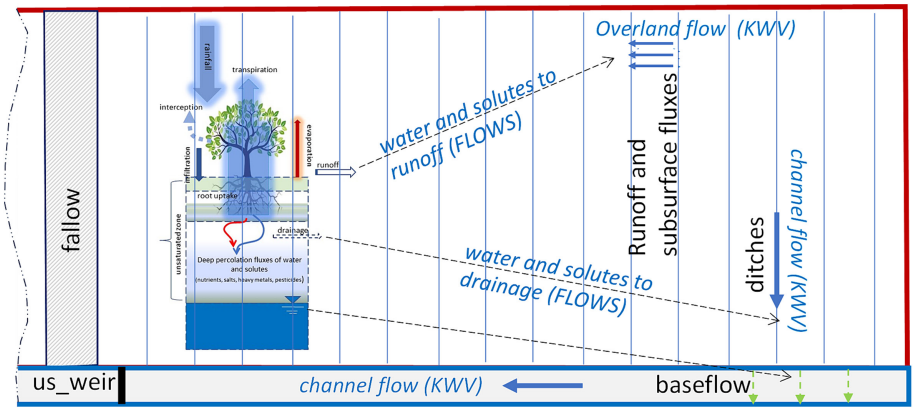

FIGURE 3 | Schematic view of the fluxes produced by FLOWS and their routing by KWV. FLOWS produces the runoff and subsurface drainage fluxes, which are routed by KWV through a sequence of overland and channel flows.

among other things, a prediction of the deep percolation flows (beyond the area explored by the root systems) of water and solutes, also making it possible to estimate the recharge of the aquifer and the transfer times of pollutants to the aquifer (e.g., nitrates, pesticides, and heavy metals). The numerical code is written in MATLAB and is based on a finite-difference solution scheme of the differential equations governing the flow of water and the transport of solutes in partially saturated porous media.

As for nutrient management, FLOWS simulates applications of organic fertilizers such as organic matter in the form of manure and crop residues, as well as mineral fertilizers. The model requires the incorporation depth of the fertilizer as input, z_{fert}. It is assumed that the fertilizer addition is uniformly distributed along the depth of incorporation. FLOWS allows us to simulate the decomposition of organic matter and the transport of carbon, nitrogen and phosphorus. In this case, the transformations of organic carbon, nitrogen and phosphorus are all controlled by the dynamics of the decomposition of the organic matter and, therefore, also by the ratios C:N and C:P. A detailed description of the model is given in Appendix A.

$$D_g^s\, D_h = \lambda v + \eta(\theta) D_0 \qquad \lambda K_{fs} = K_{\text{fom}} F_T F_{\text{mw}}^{0.5} \min\left(F_{CN} F_{CP}\right)$$

2.3.2 | The Kinematic Wave Model Applied to the Experimental Field

KWV (kinematic wave runoff routing), developed by the authors, was used for runoff routing by accounting for the influence of the channel network on the delay and the shape of the hydrograph. Kinematic wave theory is an approximation of the Saint-Venant equations, which are based on the laws of conservation of mass and momentum of shallow water flowing longitudinally and infiltrating vertically (Singh and Aravamuthan 1996; Woolhiser 1975). Kinematic wave approximation for modelling unsteady flow, gradually varied overland and channel flow assumes the bed slope, *Sb*, approximately equal to the friction slope, *Sf*, and relates the distributed, non-linear response to the drainage area and flow characteristics to the shape of the channel, the boundary roughness and the slope of the channel or overland flow surface. More details on the model are described in Appendix B.

2.4 | The Dataset for Numerical Simulations

2.4.1 | Soil Physical–Hydraulic Characteristics

A complete hydrological characterization was carried out on each of the sites selected for the installation of the MSs. Pedological pits (approximately 1.5 m × 1.5 m × 1.5 m) were excavated close to each of the MS installation sites. Site selection was based on a pedological map already available for the Sassu plain area. After pedological investigations, two undisturbed soil samples were collected from each soil horizon found up to approximately 1.5-m depth. The samples were collected using stainless-steel cylinders (inner diameter of 7.6 cm and height of 7 cm). Each soil sample was slowly wetted from below at different steps to obtain the saturation conditions. We then measured water content, θ_0, at pressure head, $h = 0$, by the gravimetric method and hydraulic conductivity, K_0, at θ_0 by the falling-head method (Klute and Dirksen 1986). The $\theta(h)$ data points were measured using a sand–kaolin suction table. Water retention experimental points were obtained at the following pressure heads: 1.0, 3.0, 7.0, 10.0, 15.0, 30.0, 70.0, 90.0, 130.0 and 180.0 cm (referring to the middle of the sample). The soil cores were oven-dried at 105°C to determine bulk density, ρ_b. Total porosity was calculated from the measured oven-dried bulk density, assuming a particle density of 2.65 g cm^{-3}. Then, soil cores were extracted from the steel cylinder and used partly to determine the water content θ at h values of 30, 60 and 120 m by the pressure membrane apparatus and partly to determine the textural characteristics.

In this work, we assumed the soil hydraulic properties to be described by the unimodal van Genuchten–Mualem model (Mualem 1976; van Genuchten 1980). The van Genuchten $\theta(h)$ relationship is expressed here in terms of the scaled water content, S_e, as follows:

$$S_e = \frac{\theta - \theta_r}{\theta_s - \theta_r} = \left[1 + \left|\alpha_{\text{vG}} h\right|^{n_{\text{vG}}}\right]^{-m_{\text{vG}}} \quad (1)$$

where α_{vG} (cm^{-1}), n_{vG} and m_{vG} are curve-fitting parameters.

Mualem's (1976) model to calculate relative hydraulic conductivity, K_r, is based on the capillary bundle theory (Childs and Collis-George 1997).

The model generally supplies reasonably accurate estimates of hydraulic conductivity from the shape of the retention curve (Luckner, Van Genuchten, and Nielsen 1989; van Genuchten and Nielsen 1985) and also for aggregated soils (Antonio Coppola 2000).

Using Mualem's model and assuming $m_{vG}=1-1/n_{vG}$, van Genuchten (1980) obtained a closed form for the hydraulic conductivity:

$$K_r(S_e)=\frac{K(S_e)}{K_0}=S_e^{\tau}\left[1-\left(1-S_e^{\frac{1}{m_{vG}}}\right)^{m_{vG}}\right]^2 \quad (2)$$

in which K_0 is the hydraulic conductivity measured at θ_0 and τ is a parameter which accounts for the dependence of the tortuosity and the correlation factors on the water content.

The data obtained on each of the four soil profiles investigated are summarized in Table 1. The last column in the table reports the dispersivity, λ, which was estimated by applying the method proposed by Scotter and Ross (1994), which deduces breakthrough curves of a tracer at a given depth for a given soil starting by the hydraulic conductivity function of that soil (see also Coppola et al. [2014] for some more details on the applied estimation procedure). Based on this approach, an average dispersivity of 2 cm was obtained, which was assumed to be uniform along the whole soil profile.

2.4.2 | Parameters for Solute Transformation and Transport Processes

Solute transformation process parameters were mostly deduced from literature data. Specifically, nitrogen transformation constants and parameters mostly came from Cabon, Girard, and Ledoux (1991), Lafolie (1991), McGechan and Wu (2001) and Shi, Zuo, and Zhang (2007). As for phosphorus, the kinetic constants and other parameters are taken from Mansell, Selim, and Fiskell (1977) and Mansell, Selim, Kanchanasut, et al. (1977). The parameters for solute transformation and transport are reported in Table 2. In the table, K_{ru} (–) are factors for solute root uptake, accounting for a positive or negative selection of solute ions relative to the amount of root water uptake.

2.4.3 | Parameters for Kinematic Wave Simulations

Table 3 summarizes the parameters used for routing of the excess water (drainage and direct subsurface drainage to ditches), along with the dissolved solutes, to the surface drainage network. Some of them reflect the regular geometry of the experimental field (see Figure 1), such as the width and length of the elemental fields, length of ditches and length of secondary drainage channel. The slope and roughness of each of the drainage network segments was also assumed to be uniform.

The table also reports solute dispersivity. In the case of overland flow, a constant and uniform dispersivity of 10 cm was assumed based on the study from Abbasi et al. (2003). As for ditch and channel dispersivity, the Fischer equation (Fischer et al. 1979) was considered for deducing the solute longitudinal dispersion, D_x, from the cross-sectional mean flow velocity, u, and the shear velocity, $\breve{u}=\frac{\sqrt{g}}{C}u$, with C as Chezy's coefficient and g as the gravitational acceleration, and from the geometric characteristics of the flow section (width, w, and water depth, y). By neglecting diffusion, D_x is related to λ_{rn} as $\lambda_{rn}=D_x/u$.

2.5 | Numerical Simulations

2.5.1 | Flow Field and Top- and Bottom-Boundary Conditions

Simulations were carried out for a 2-year period, from 1 January 2021 to the end of 2022, for which a complete dataset was available. A soil profile of 100-cm depth was considered. By looking at Table 1, it is apparent how the hydrological characteristics of the soil profile close to the MS1 and MS2 monitoring sites are very similar, even in terms of horizon thicknesses. The same may be observed for the soil profiles in MS3 and MS4. This is why, in carrying out the simulations, we averaged the MS1 and MS2 soil profile parameters to describe the hydrological behaviour of the downstream field (DsF) and the MS3 and MS4 profile parameters for the upstream field (UsF). Due to the very shallow groundwater, based on the tensiometric readings, a hydrostatic soil profile was assumed along the whole soil profile.

As for the water top-boundary conditions, simulations accounted for rainfall measured by a micrometeorological station installed in the area, very close to the experimental field. Registered irrigation volumes and potential evapotranspiration fluxes, ET_p, were also used as the variable top-boundary condition. ET_p fluxes were calculated according to the reference evapotranspiration, ET_r, method. The Penman–Monteith equation (Allen et al. 1998) was first used to calculate the ET for the reference crop. Thus, the ET_p for the specific crops simulated in this study were calculated as $ET_p=kc\times ET_r$ with kc being a crop factor, which depends on the crop type and the growth stage. ET_p was thus partitioned into T_p and E_p on the basis of Beer's law (Ritchie 1972):

$$\begin{aligned} E_p&=ET_p\times e^{-k\times LAI}\\ T_p&=ET_p-E_p \end{aligned} \quad (3)$$

For all the simulations, the LAI measured under the different salinity treatments, along with an extinction coefficient of 0.45, was used to calculate the potential transpiration, T_p, from ET_p.

TABLE 1 | Pedological and hydraulic characteristics of the four soil profiles investigated in this study.

Soil classification	Horizon	Depth (cm)	Sand	Silt %	Clay	ρ_b (g/cm^3)	θ_0	θ_r	α_{vG} (1/cm)	n_{vG}	K_0 (cm/day)	λ (cm)
MS1—*Vertic Haploxerepts*	Ap	55	14.7	27.2	58.1	1.25	0.405	0.099	0.018	1.137	2.90	2.0
	Bg	115	2.8	24.1	73.1	1.30	0.412	0.106	0.020	1.197	3.50	2.5
	Cg	150	6.0	21.0	73.0	1.36	0.510	0.104	0.020	1.189	5.10	2.5
MS2—*Vertic Haploxerepts*	Ap	55	20.9	26.9	52.2	1.27	0.423	0.095	0.018	1.146	3.40	3.0
	Bg	100	7.5	21.5	71.0	1.27	0.419	0.103	0.020	1.193	2.50	2.6
	Cg	150	6.0	21.0	73.0	1.36	0.515	0.104	0.020	1.189	4.30	2.0
MS3—*Aquic Xeropsamments*	Ap	70	14.7	24.2	61.1	1.29	0.410	0.099	0.019	1.189	4.10	2.1
	2Cg	110	85.7	1.7	12.6	1.42	0.460	0.061	0.026	1.813	90.64	3.6
	3Cg	150	56.0	4.0	40.0	1.57	0.394	0.081	0.028	1.150	3.70	3.6
MS4—*Typic Fluvaquents*	Ap	75	16.7	24.9	58.4	1.26	0.400	0.098	0.019	1.228	4.80	2.0
	2Bw	100	91.0	2.0	7.0	1.32	0.450	0.058	0.029	1.670	101.98	3.1
	3Cg	160	67.7	3.7	28.6	1.55	0.374	0.070	0.026	1.190	5.80	3.4

TABLE 2 | Parameters for solute transformation and transport processes simulated in this work by FLOWS.

	K_{ads} N-NH_4	K_{ads} N-NO_3	K_{nitr}	K_{imm}	K_{dntr}	D_0 N-NH_4	D_0 N-NO_3	K_{ru} N-NH_4	K_{ru} N-NO_3
	(cm^3/g)	(cm^3/g)	(1/day)	(1/day)	(1/day)	(cm^3/day)	(cm^2/day)	(–)	(–)
	0.100	0.000	0.500	0.020	0.030	1.710	1.640	0.100	1.000
Phosphorus	K_{ads1} P-PO_4	K_{ads2} P-PO_4	K_{prc1} P-PO_4	K_{prc2} P-PO_4	K_{chs1} P-PO_4	K_{chs2} P-PO_4	D_0 P-PO_4	K_{ru} P-PO_4	
	(cm^3/g)	(cm^3/g)	(1/day)	(1/day)	(1/day)	(1/day)	(cm^2/day)	(–)	
	0.100	0.010	0.050	0.010	0.005	0.001	0.530	0.300	

The T_p values were distributed over the root zone according to a uniform root density distribution, even if any root density distribution may be used in the code according to a specific crop being simulated. A maximum root depth was considered for all the crops considered, increasing from 0 to 80 cm during the crop growth season.

A pressure head (Dirichlet) variable bottom-boundary condition was assumed at 100 cm, based on the tensiometric readings' evolution over time. The spatial flow field was discretized in 100 nodes of constant width (Δz). Time discretization starts with a prescribed initial time increment (Δt). This time increment was automatically adjusted at each time level according to a solution convergence criterion (Coppola et al. 2011, 2012, 2015, 2019a).

2.5.2 | Irrigation and Fertilizer Applications

Figure 4 shows the water coming to the experimental field by both rainfall and irrigation supplies during the 2-year period of simulations. During the first year, melon was irrigated by drip irrigation whereas corn was irrigated by sprinkler irrigation. In the case of drip irrigation, drippers of 2 L/h were installed at a distance of 30 cm in-line and 70 cm between lines. Due to the low conductivity of the upper layer and the volume and frequency of irrigations (about 5–15 mm each day), the soil surface between the dripper lines moistened almost completely, so as to establish a quasi-1D vertical flow, justifying the use of a 1D model for describing both water and solute transport even in the DsF.

As for the nutrient supplies to the crops, only inorganic fertilizers were used. Consequently, the OM decomposition and mineralization were not simulated. Table 4 reports the nutrient applications in kilogrammes per hectare during the year 2021, when the DsF was cultivated with melon and irrigated by drip irrigation, whereas the UsF was cultivated with corn. As already mentioned, in 2022, both fields were cultivated only with corn, and the fertilizers applied and the application dates were approximately as those reported in the bottom part of the table for the year 2021.

3 | Results and Discussion

This section shows and interprets (also by modelling) the measurements made using the monitoring system installed in the experimental field. As mentioned, the analysis was carried out considering the average of the measurements carried out in MS1 and MS2 for the DsF and the average of the measurements carried out in MS3 and MS4 for the UsF. The same distinction in DsF and UsF was also maintained for 2022, the year in which the two fields were both destined for corn cultivation.

To make the time evolution of the different sensor readings clearer, most of the figures presented below will also show the time distribution of rainfall events and irrigation applications during the 2 years of monitoring.

TABLE 3 | Parameters used in this work for simulation of overland and channel flows simulated by KWV. For a clear understanding of the parameters, the table can be compared to the experimental scheme given in Figure 1.

Parameter	Abbreviation (units)	Value
Field plain width	WF (m)	200
Field plain length	LF (m)	25
Ditch length	LD (m)	200
Partial channel length	LCp (m)	25
Field plain slope	SLP_F	0.010
Ditch slope	SLP_D	0.005
Channel Slope	SLP_C	0.001
Manning roughness coefficient in the field	n_f_F (d m$^{-1/3}$)	0.03
Manning roughness coefficient in the ditch	n_f_D (d m$^{-1/3}$)	0.025
Manning roughness coefficient in the channel	n_f_C (d m$^{-1/3}$)	0.020
Overland dispersivity	λ_{rn}_F (cm)	10
Ditch dispersivity	λ_{rn}_D (cm)	From Fischer et al. (1979)
Secondary channel dispersivity	λ_{rn}_C (cm)	

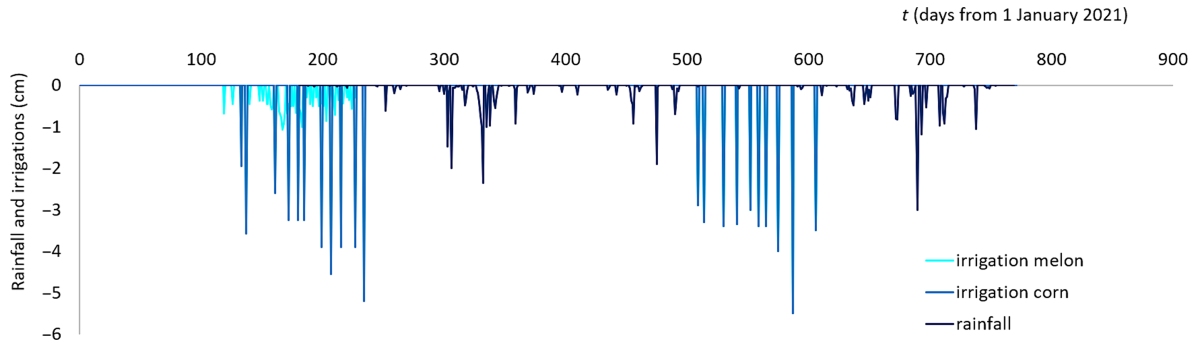

FIGURE 4 | Rainfall and irrigation supplies during the 2-year period of simulations. Note that the first-year irrigation involved both melon into the DsF and corn into the UsF.

3.1 | Pressure Head Measurements

As mentioned, each of the four MS was equipped with two tensiometers, installed approximately at depths of 80 and 110 cm. The graph in Figure 5 shows the trend of the pressure heads observed respectively in the UsF and DsF. In both cases, the pressure head shown refers to the average of the two potentials observed at the two installation depths of the tensiometers and of the two MSs in each field.

First of all, during the first year of monitoring, the pressure head value at a depth of about 90 cm was always either larger than or close to 0 during most of the irrigation season, indicating saturated conditions well above the tensiometer readings. This was especially verified in the case of melon cultivation in the DsF, where, even if the crop was irrigated with a dripper irrigation system, the irrigation volumes were evidently enough to induce saturation conditions up to the ditches bottom (about 60-cm depth), so as to activate them and keep the pressure head at a maximum positive value of about 30–35 cm. In any case, at the end of the irrigation season, when irrigation contributions stopped, the pressure heads decreased progressively down to negative values, even if still close to saturation.

In the case of corn, irrigated by a sprinkler system, the pressure head observed in the first monitoring year in the UsF assumed positive values only during the first year of monitoring, sometimes at 15–20 cm, indicating a regular presence of conditions of saturation or close to saturation starting at about 60–70 cm from the soil surface. Compared to the drip irrigation, after the

irrigation season, the pressure head in the sprinkler-irrigated fields was more dynamic, and the pressure head values decreased up to about −50 cm.

TABLE 4 | Nutrient applications during the year 2021. For 2022, the dates and the nutrient amounts are approximately the same as for corn in 2021 for the whole field, with an additional background nitrogen fertilization at 400 days from 1 January 2021. The values in the table are in kilogrammes per hectare.

Days from 1 January 2021	Melon		Corn	
	kg N/ha	kg P/ha	kg N/ha	kg P/ha
99	13.33	40.00		
122	1.04	3.20	21.60	54.00
130	2.08	6.40	110.40	
140	3.31			
148	2.40	12.20		
158	4.00	4.00		
168	4.00	4.00		
173	1.73			
178	1.73			
199	4.00	4.00		
210	2.60	2.60		
	Corn		**Corn**	
400	90.00		90.00	

As will be shown later (see Section 3.4), the different behaviours between melon and corn fields can be mostly ascribed to the different irrigation systems in the DsF and UsF and only partly to some differences in the soil profile and the corresponding hydraulic properties. In the case of melon, the drippers' flow rate was such that it allowed all the irrigation water to infiltrate into the soil profile, which induced a water table rising up to the ditches.

Differently, in the case of corn, the sprinkler flow rate induced some direct runoff at the soil surface, which limited the surface water infiltration and allowed a lower deep infiltration of water. This will be also evident later by looking at the water content evolution measured by the CS655 probes.

In general, by comparing the pressure head evolution in the two fields, a different dynamic can be observed in the two fields during the autumn–winter of both the monitoring years, when the fields received only rainfall water. Specifically, the pressure head in the UsF decreases more than that observed in the DsF, where the pressure head remains quite close to saturation, with values not lower than −15 cm. This may be partly ascribed to the different hydrological behaviours of the whole soil profile. However, this also shows that the quite high pressure head values reached with the drip irrigation in the DsF cultivated with melon (the period between 170 and 220 days) may likely be ascribed to the fact that, in the DsF soils, the irrigation already starts with positive pressure heads at 90-cm depth.

From the perspective of runoff generation and kinematic wave simulation for runoff routing, during the first year, the two fields produced excess water, to be drained by the irrigation

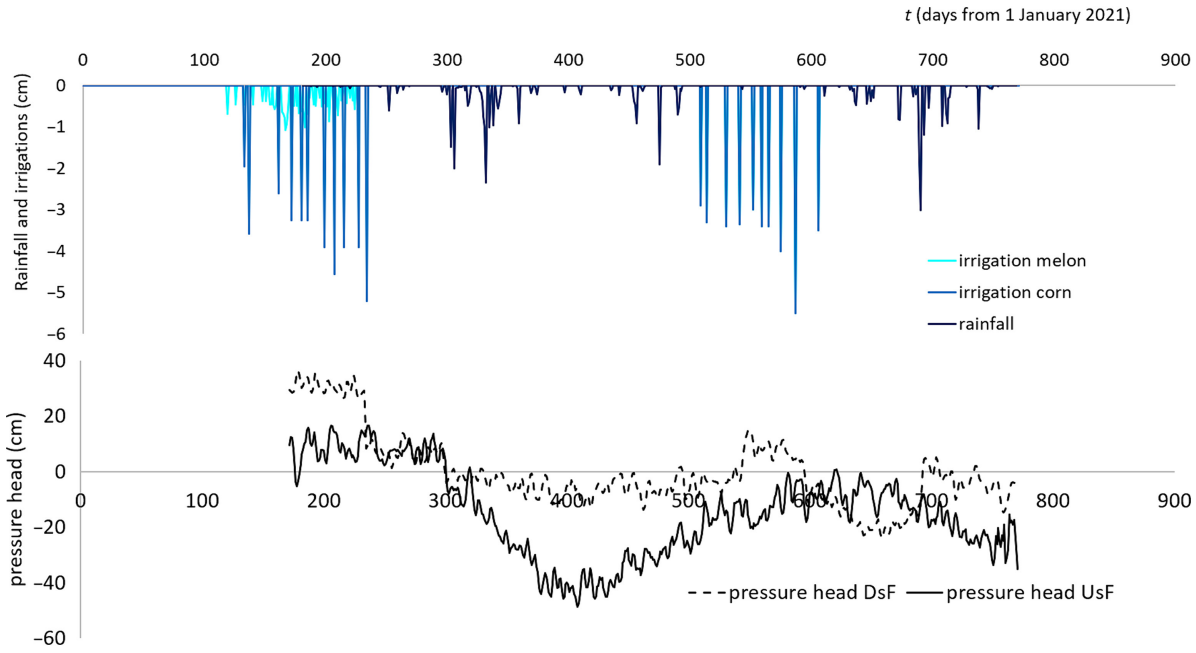

FIGURE 5 | (Bottom) Average pressure heads (at $z = 90$ cm) calculated from the four tensiometer readings observed in the two MSs for both the UsF and DsF. (Top) Rainfall and irrigation supplies in 2021 and 2022. During 2021, the irrigation concerned both the melon, irrigated with a dripper irrigation system (data in light blue in the graph), grown in the DsF, and the corn crop, irrigated with sprinklers (data in blue in the graph) and grown in the UsF. Precipitation is shown in dark blue. In 2022, the irrigations concerned only the corn which occupied both fields.

network, with two different mechanisms: (1) the UsF generated surface runoff by a Hortonian mechanism, so that the sprinkler flow rate overcame the soil infiltration capacity. In this case, the runoff reached the ditches after flowing over the field. The runoff to the ditches was simulated as overland flow in the KWV model; (2) the DsF produced supplied excess water directly to the ditches by subsurface lateral drainage. In the KWV, this excess water was added as distributed input directly to the ditches' flow.

The fact that the relatively high positive pressure head values in the DsF during the first year were mostly attributable to the irrigation system is confirmed by looking at the second year of monitoring, when both the fields were irrigated by sprinkler irrigation. In this case, the pressure head at $z = 90$ cm in the DsF was limited to 10–15 cm. In any case, the dynamics of the pressure head in the two fields was quite different, and this is to be ascribed rather to the different layering of the soil profile and their corresponding hydrological behaviour.

The pressure head evolution shown in the figure served to establish the variable head condition at the bottom-boundary of the flow domain simulated by FLOWS.

3.2 | Measured and Simulated Water Contents

Figure 6 shows the water contents at the five measurement depths in the DsF and UsF. Measurements started from Day 172. For greater clarity, the evolution over time of the water content at depths of 10 and 30 cm has been represented in separate graphs against the water contents at greater depths. Again, the irrigation applied in 2021 and 2022, as well as the rainfall, is also shown at the top of the graph.

From the comparison between the graph of the inputs (irrigations or rainfall) and the dynamics of the water contents, it can be observed how the readings made with the CS655 sensors (dashed lines in the graphs) are extremely sensitive to any input on the surface. This was particularly evident at the first two depths (10 and 30 cm), whereas the measurements at greater depths showed a much more attenuated dynamic and always around the water content at saturation, as was to be expected by observing the water potential measurements at 90 cm, which, as mentioned, indicate a condition of a porous medium close to the saturation.

As for simulations by FLOWS, in general, they reproduced the dynamics observed at the first two depths with good accuracy. At greater depths, the model predicts fairly stable values of water content, sometimes failing to follow the dynamics, however limited to 0.02–0.03 cm^3/cm^3, recorded in certain periods (e.g., in the UsF in the period between 300 and 500 days) by the water content sensors. However, these dynamics are not relevant for the purposes of the overall water balance in the soil profile. However, it should be considered that, in all the simulations, FLOWS was used in a forward configuration, using the measured hydraulic properties of the soil (see Table 1), with the top-boundary conditions being measured in terms of rainfall and irrigation volumes and those at the bottom boundary being measured with tensiometers (see Figure 5) without calibration.

3.3 | Measured and Simulated Soil Electrical Conductivity

The graphs in Figure 7 show the time evolution of bulk electrical conductivity, EC, measured by the CS655 sensors at five different depths (the same as the water contents) in the two fields.

It is worth to note how the EC behaviour closely reflects that observed in the water content (see Figure 8). It is especially important to understand the extent to which the nitrate eventually transported by the water transport is responsible for changes in the EC at higher depths. In this sense, Figure 8 reports the EC curve measured at 90 cm for both the DsF and UsF, along with the water content observed by the same sensors at the same depth.

For a better interpretation of the CS655 probe readings, the figure also shows the EC measured by the multiparametric probe in the piezometer installed at the MS4 (and thus in the UsF) at a depth from the soil surface of 150 cm. Unfortunately, the data coming from the EC sensor in the piezometer installed in the DsF did not work, and thus, data are not shown here. From the curves, it is apparent how most of the EC dynamics may be ascribed to the changes in the water content, whereas the EC in the piezometer showed low fluctuations around 3 dS/m. Later, we will show that these fluctuations correspond to low nitrate fluctuations around 15 mg/L, which will be assumed as a background concentration in the groundwater and, as such, used in the KWV solute transport simulations. In any case, these fluctuations indicate a quite insignificant arrival of nutrients to the water table. Again, this may be explained by the two different excess water production mechanisms acting in the DsF and UsF.

In DsF, during the first year of monitoring, the activation of the ditches is likely to be responsible for the displacement of water (and dissolved solutes) as soon as it reaches the very shallow water table. In this sense, it is well known how artificial drainage is commonly (and rightly) considered to produce and enhance pollution of surface water by nutrients and other agricultural diffuse-source contaminants (see, e.g., Jaynes and Isenhart 2014).

In the UsF, nutrients (including nitrogen, in the forms of both $N\text{-}NH_4$ and $N\text{-}NO_3$) are lost mainly through runoff production. Actually, the sprinkler irrigation rate overcomes the soil infiltration capacity, producing significant water fluxes to the runoff. Nutrients (both nitrogen and phosphorus) in the upper soil layer diffuses to the runoff water and are transported by overland flow.

In summary, these are the two main mechanisms of pollution transport to surface waters identified in the experimental field (and likely to operate in the whole Sassu plain agricultural area). By contrast, the area would be characterized by reduced

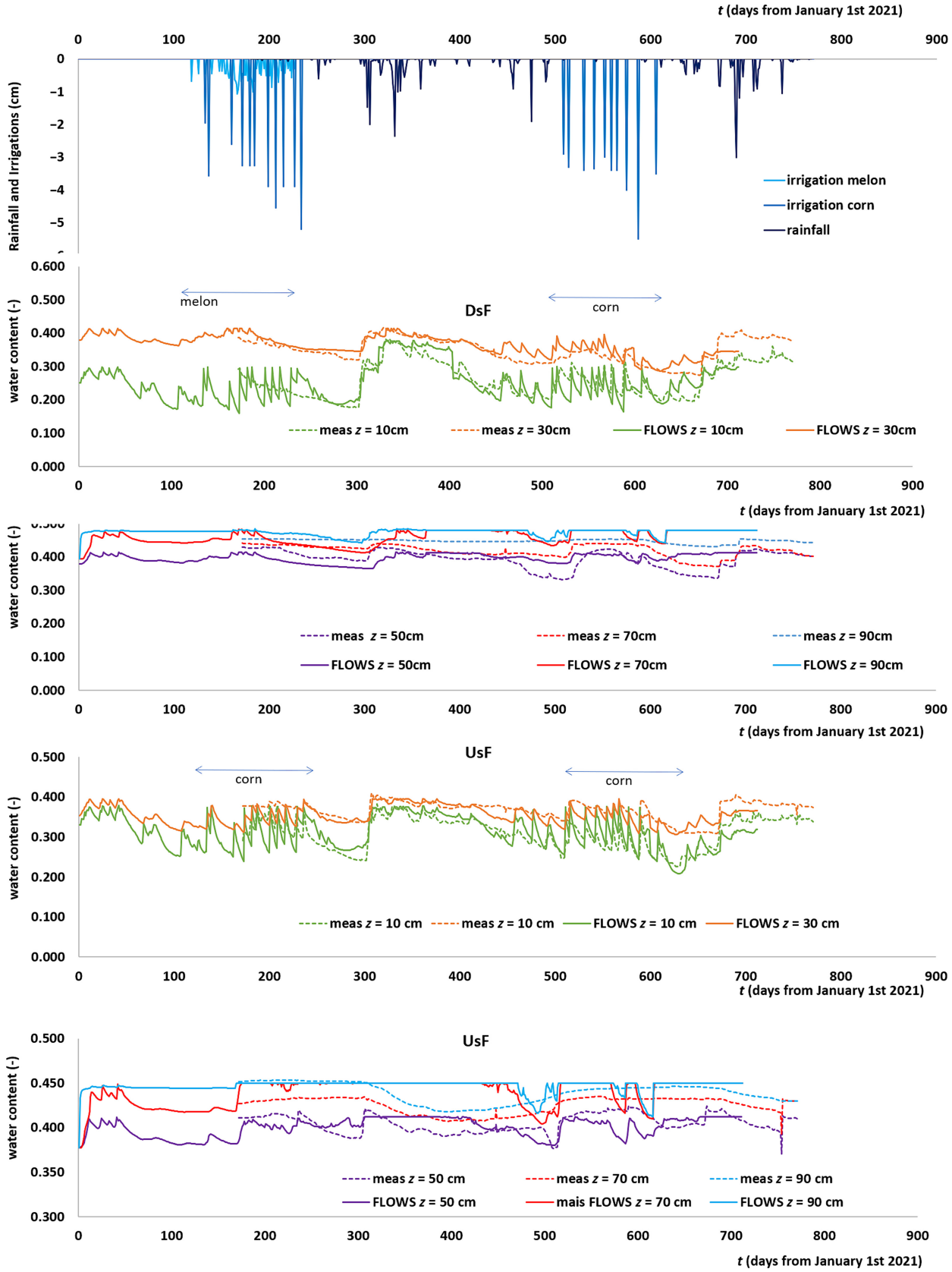

FIGURE 6 | Water contents at five different depths in the DsF and UsF. The time evolution of the water content at depths of 10 and 30 cm was represented in separate graphs against the water contents at the greatest depths. The irrigation in 2021 and 2022 is also shown at the top of the graph, along with the rainfall events.

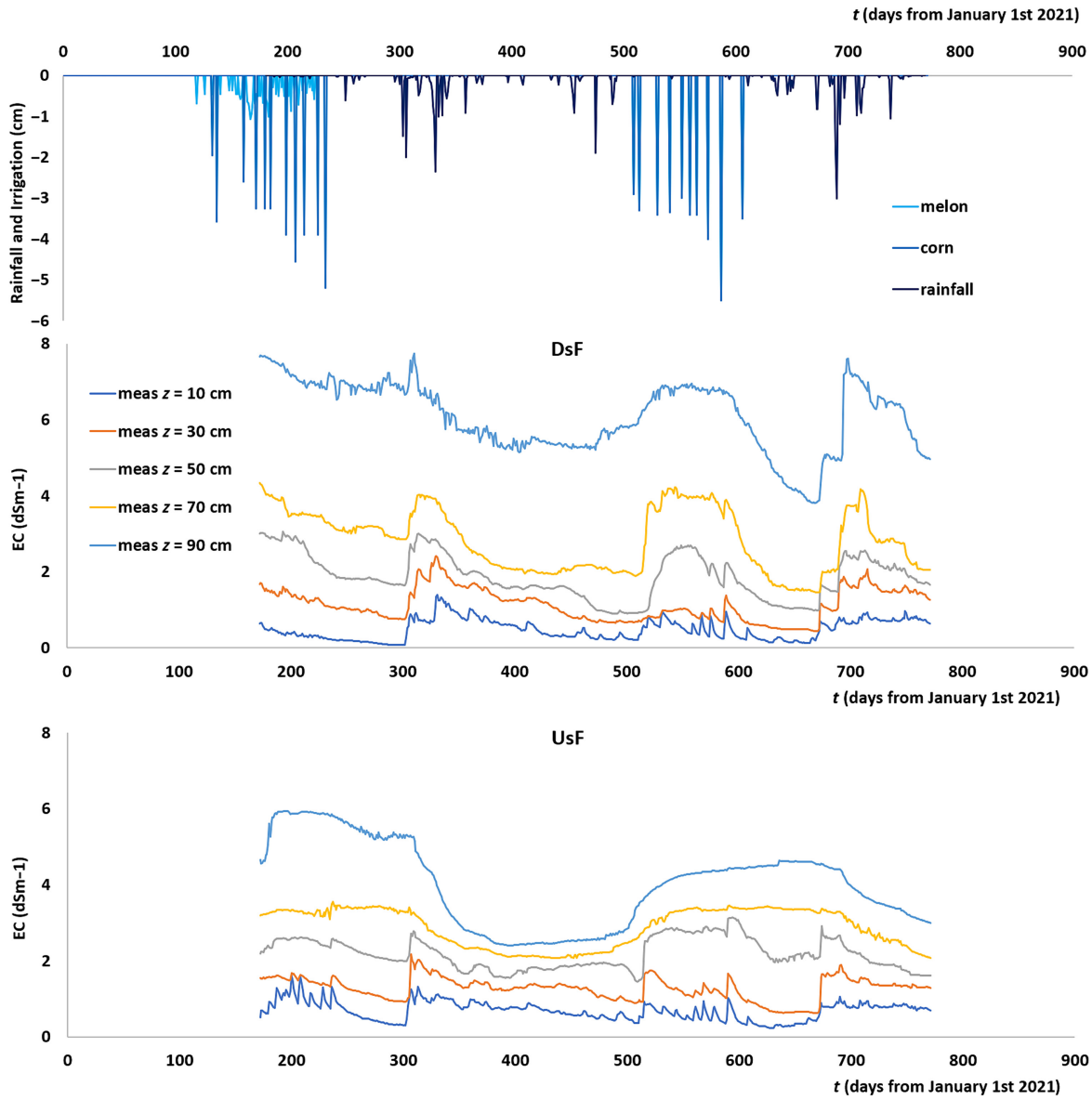

FIGURE 7 | Time evolution of bulk electrical conductivity measured by the CS655 sensors at five different depths in both the DsF and UsF.

nutrient losses to groundwater, despite the very low depth to the water table characterizing the area.

3.4 | Nitrogen and Phosphorus Runoff and Concentrations in the Secondary Drainage Channel: Measurements and Simulations

FLOWS simulations produced the fluxes of water (in centimetres per day) and of solutes (in grammes per square centimetre) towards the surface runoff (runoff), as well as to the lateral drainage. As an example, the graphs in Figure 9 report water and solute fluxes generated by FLOWS for one of the elementary fields in both the UsF and DsF for the year 2021. Specifically, Figure 9a–c shows the water, the N-NO_3 and the P-PO_4, respectively, to (1) runoff in the UsF which was cultivated with corn and irrigated by a sprinkler irrigation system in 2021 (left *Y*-axis) and (2) the subsurface lateral flow in the DsF which was cultivated by melons and irrigated by a drip irrigation system during the same year (right *Y*-axis). Figure 9d shows the P-PO_4 to the subsurface fluxes at the DsF. Note the relatively high N-NO_3 and P-PO_4 peaks for the field in the DsF. As the high peak in the phosphorus graph hid the dynamics of P-PO_4 in the runoff during both the summer and winter periods, Figure 9d reports again the same graph as in Figure 9c with a vertical axis scale changed to see those dynamics.

Once the fluxes of water and solutes to runoff and lateral drainage were generated with the FLOWS model, these fluxes were passed as input to the KWV model for their routing. The KWV model produced the simulated water and solute hydrographs to be compared to those measured along the secondary drainage channel, precisely at the control sections corresponding respectively to the *us_weir* installed in correspondence with MS3 (see Figure 1), which only intercepts the flows of water and solutes from the *UsF*, and to the *ds_weir* installed at MS1, which

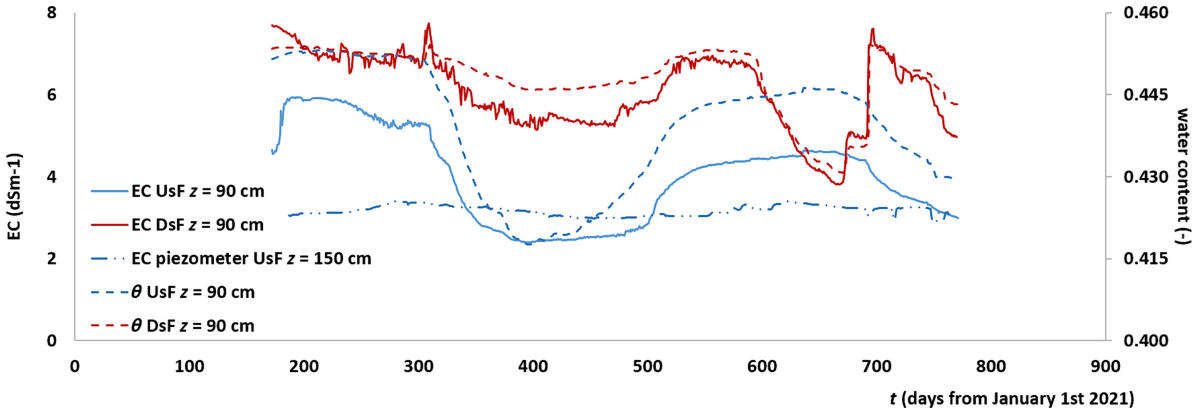

FIGURE 8 | Time evolution of bulk electrical conductivity and water content measured by the CS655 sensors at 90-cm depth in both the DsF and UsF. The figure also shows the EC measured in the piezometer installed in the UsF.

intercepts the flows from the entire experimental field (*UsF* plus *DsF*).

Figure 10 shows the simulated water and solute runoff and subsurface lateral flow in the different compartments of the drainage network for both the *UsF* and *DsF* and for the whole simulation period including the years 2021–2022. Specifically, Figure 10a1 reports the water runoff generated by FLOWS in the UsF. Figure 10a2 reports the water subsurface lateral flow in the DsF for the first year, when DsF was cultivated with melon and irrigated by a drip irrigation system, and then the water runoff in the DsF in the second year, when it was cultivated with corn and irrigated with a sprinkler irrigation system. Therefore, Figure 10b1,b2 shows the water and nitrate overland flow (and subsurface lateral flow for the first year in the DsF) over the single elementary field, Figure 10c1,c2 shows the water and nitrate runoff (and subsurface lateral flow for the first year in the DsF) along the single ditch, and the graphs Figure 10d1,d2 shows the water fluxes and nitrate concentrations along the channel, respectively, at the *us_weir* and *ds_weir* monitoring sections. Finally, Figure 10e1,e2 provides the cumulative water volumes and nitrate mass passing thorough the two weirs. In these last graphs, the cumulative measured water volumes and solute mass are also shown, for the sake of comparison with the simulations. Note that although the concentrations in the DsF is very high in the first year, its contribution to the total solute mass in the secondary channel is quite low because of the low water discharges, which came from subsurface fluxes when the field was irrigated by a drip irrigation system.

Note in Figure 10b1,b2 the very high concentrations coming from the melon field (DsF) during the first year of simulation (2021), which are related to the relatively low water fluxes coming from the same field compared to the UsF. We recall that in 2021, the DsF was irrigated by drip irrigation, whereas in the second year (2022), the DsF was irrigated by sprinkler irrigation. As already discussed in Section 3.1, the lower fluxes in 2021 from the DsF have to be attributed mostly to the irrigation system rather than the soil profile characteristics. This is demonstrated by observing that, once the DsF was irrigated by sprinkler irrigation and cultivated by corn, it produced water runoff and solute concentrations similar to the UsF (see the second year of simulations in the graphs in Figure 10b1,b2).

In general, if we look at Figure 10e1,e2, the model was able to mostly predict the overall observed water volumes and nitrate mass passing along the secondary channel. Note that this result was obtained mainly by manually changing the resistance coefficient, n_f, in the KWV model.

For further details, Figure 11a shows the evolution over time of the electrical conductivity measured by the multiparameter probes installed at the *us_weir* and *ds_weir*. The graph also reports the N-NO_3 concentration as measured in the UsF by the multiparametric probe installed in the MS4. Figure 11b shows the concentration of nitrate measured (symbols) using the ion-specific electrode supplied with the two multiparametric probes. Finally, Figure 11c shows the phosphorus concentrations measured by periodically sampling the channel water in correspondence to the weirs and analysed by the photometric method. In both the nitrogen and phosphorus graphs, the solid lines represent the simulations obtained using the FLOWS outputs in a model based on the kinematic wave model for the simulation of surface transport ('routing') of surface outflows and dissolved solutes and already shown in Figure 10d1,d2. Note that, for phosphorus, no background concentration was assumed in the baseflow contribution.

The nitrate measurements are limited to a period of about 400 days (for the *us_weir*) and 350 days (for the *ds_weir*), as there were later problems in the functioning of the ion-specific electrodes, likely because of some sludge incrusting the sensors, though they were regularly cleaned and recalibrated using reference solutions of known concentration. Missing nitrate measurements may also be observed in the period of 330–400 days. In this period, due to relatively intense rainfall, some water back-flows were observed from the main drainage canal to the secondary drainage channel (see Figure 1), thus temporarily altering the concentrations in the channel. To avoid confusion in data interpretation, the measurements in that period were thus excluded from the graph.

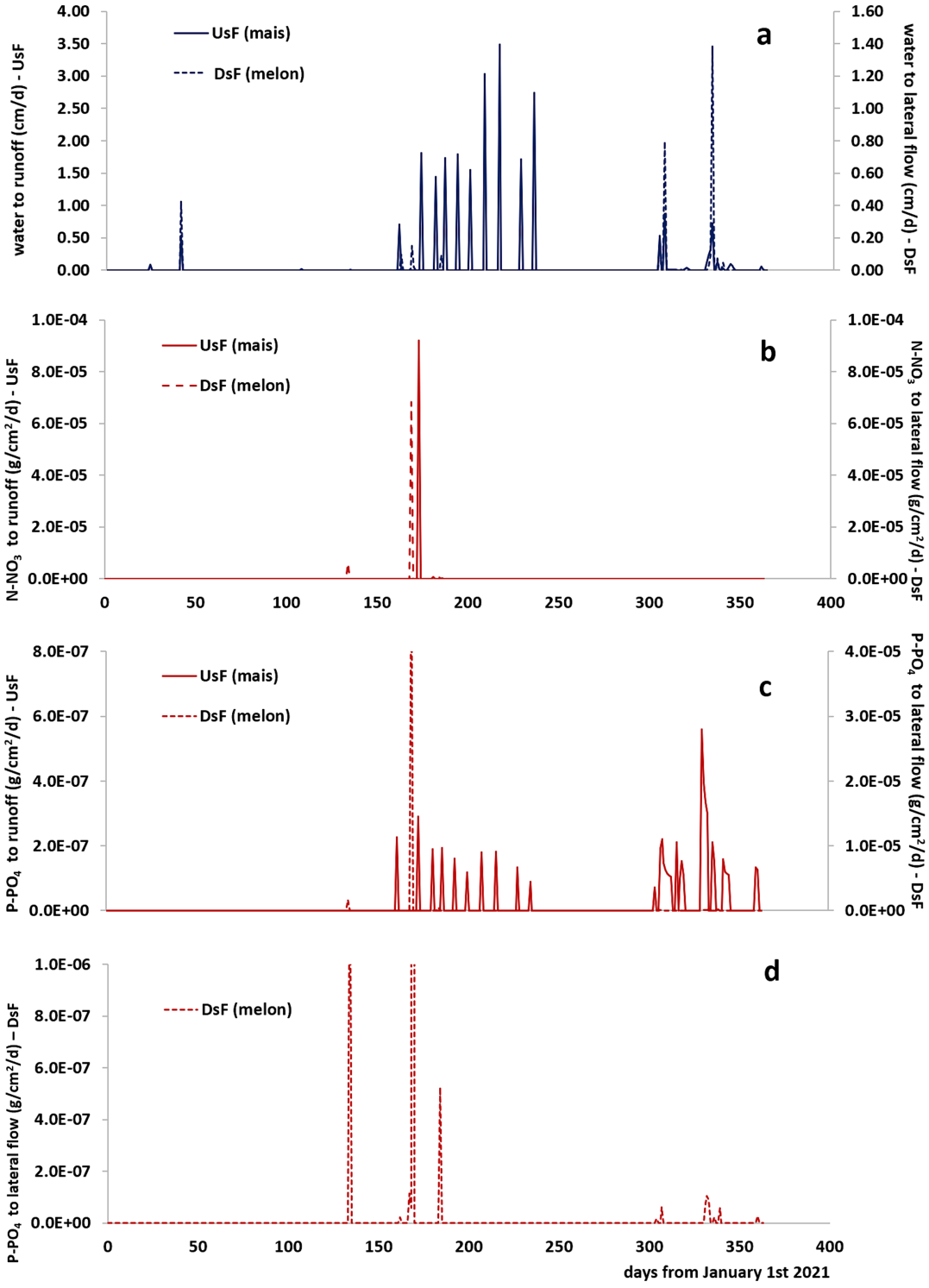

FIGURE 9 | Water and solute fluxes generated by FLOWS for one of the elementary fields in both the UsF and DsF for the year 2021. Specifically, Graphs (a), (b) and (c) show the water, the $N\text{-}NO_3$ and the $P\text{-}PO_4$, respectively, to (1) runoff in the UsF, which was cultivated with corn and irrigated by a sprinkler irrigation system in 2021 (left *Y*-axis), and (2) the subsurface lateral flow in the DsF, which was cultivated by melon and irrigated by a dripper irrigation system during the same year (right *Y*-axis). Graph (d) simply reproduces Graph (c) but with a rescaled *Y*-axis to show up the dynamics of phosphorus fluxes to the lateral subsurface flow in the DsF in both the summer and winter periods, hidden by the high peak in Graph (c).

In any case, the available period of observations covered with good detail the evolution of nitrate in the secondary drainage channel, coming from the fertilizations supplied during both the 2021 and 2022 irrigation seasons. In general, the concentration observations at the weir's sections in the channel reveal that the solute entering the runoff reaches the end section of the secondary channel very late. As discussed in Section 2.3.2, this behaviour is reasonably the result of intermittent and nonuniform flow, which in principle

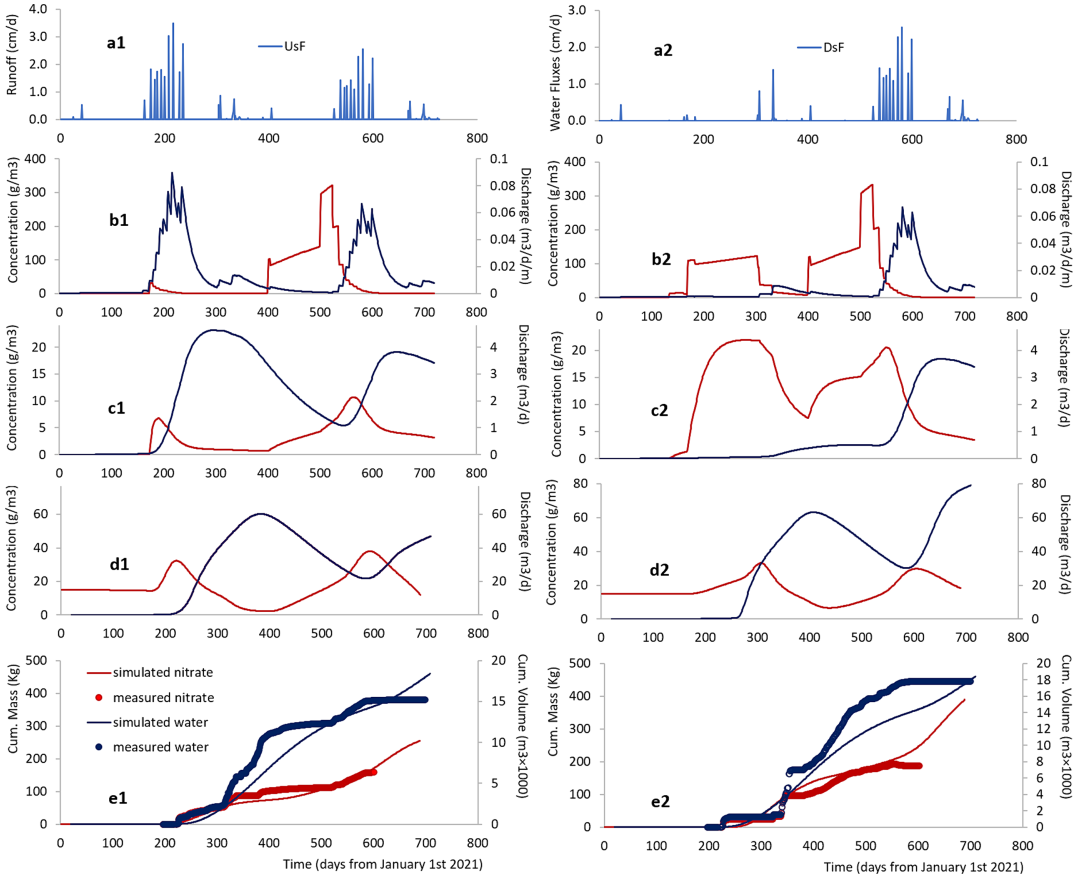

FIGURE 10 | Simulated water runoff and subsurface lateral flow (blue lines) and solute runoff (red lines) in the different compartments of the drainage network for both the *UsF* and *DsF* and for the whole simulation period including the years 2021–2022. Specifically, Graph (a1) reports the water runoff generated by FLOWS in the UsF. Graph (a2) reports the water subsurface lateral flow in the DsF for the first year, when DsF was cultivated with melon and irrigated by a drip irrigation system, and then the water runoff in the DsF in the second year when it was cultivated with corn and irrigated with a sprinkler irrigation system. Graphs (b1) and (b2) are for the water and nitrate overland flows (and subsurface lateral flow for the first year in the DsF) over the single elementary field, Graphs (c1) and (c2) are for the water and nitrate runoff (and subsurface lateral flow for the first year in the DsF) along the single ditch and Graphs (d1) and (d2) are for the water fluxes and nitrate concentrations along the channel, respectively, at the *us_weir* and *ds_weir* monitoring sections. Finally, Graphs (e1) and (e2) provide the cumulative water volumes and nitrate mass passing thorough the two weirs.

cannot be reproduced by the kinematic wave approach. Moreover, the KWV model does not consider the possible nitrate transformations during the routing time. And yet, pragmatically coupling FLOWS with KWV still allows a quite faithful reproduction of the evolution of the observed nitrate concentration, albeit with a much smoother trend given the difficulty of being able to model all the variability of the paths actually followed from the runoff. In this sense, as the matching of the KWV curves with measurements was obtained by only tuning the resistance parameter (n_f in Equation B2 in Appendix B), the latter should not be interpreted anymore as a uniform flow resistance parameter, as it also accounts for all the possible changes in nitrate mass not explicitly considered in the KWV model and for the very delayed flow indicated by the observations.

Overall, the nitrate concentrations reach peaks of the order of 30–40 mg/L (30–40 g/m^3), corresponding to a total nitrate mass coming from the field of the order of 10–15 kg and given the water discharges ranging between 10 and 87 m^3/day simulated by KWV in the same period. The early rising before the second nitrate peak is due to the nitrogen fertilization at about 400 days (see Table 4). It should be noted that the curves in the graph show a background concentration (both measured and simulated) of about 15 mg/L, which is the average concentration measured in the UsF piezometer (see Figure 10a, top graph) and which was used in the KWV as the background concentration for the baseflow, that is, the water draining steadily to the secondary drainage channel directly from the shallow groundwater. Note that the baseflow was not simulated directly in KWV but was assumed as a steady flow at a constant concentration to the secondary channel.

The bottom graph in Figure 10 reports the P-PO_4 evolution measured by the photometric method (symbols) and simulated by the KWV model. Measurements were taken periodically in the period of 200–600 days. The same parameters used for the nitrogen routing were also able to reproduce the phosphorus measurements quite adequately.

4 | Discussion and Conclusions

Agriculture activities are known to be the main diffuse source of pollutants (nutrients, pesticides, ...) to groundwater and

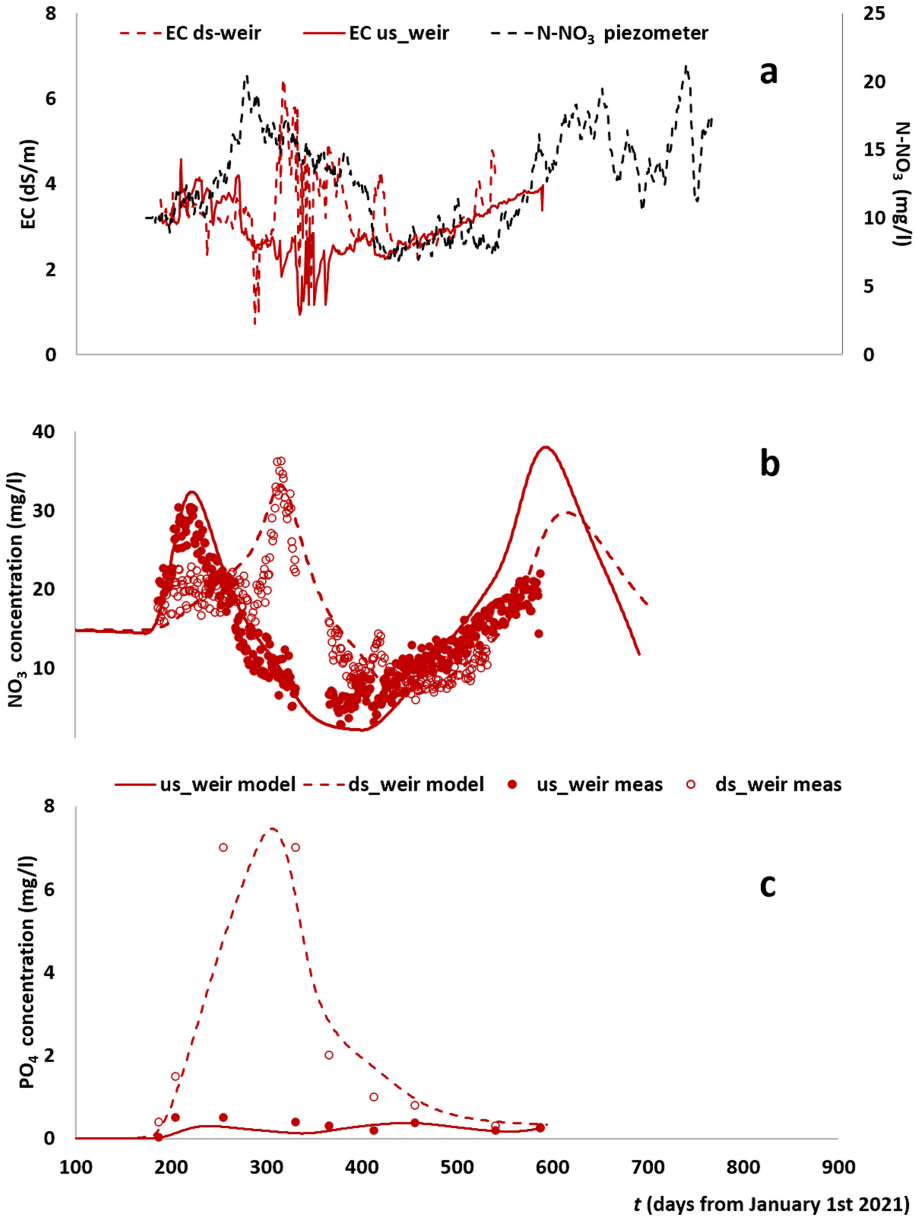

FIGURE 11 | (a) Electrical conductivity, EC, measured by the multiparametric probes installed close to the us_weir and ds_weir and N-NO_3 measured in the piezometer installed in the MS4 (UsF); (b) nitrogen concentration as measured (symbols) by ion-selective electrode; (c) phosphorus concentration as measured (symbols) by photometry. Solid lines refer to the simulations carried out by combining FLOWS (for water and solute fluxes to runoff and lateral drainage) and KWV (for water and solute routing).

surface waters, and their ecohydrological impact is widely documented. Many European directives (Water Directive, Nitrates Directive, Pesticides Directive, ...) were just originated from the need to improve the qualitative status of polluted water bodies and introduce increasing constraints in the management of fertilizers and irrigation water at different levels (from farm to whole irrigation district scales). However, based on decades of experience, it is now evident that a unique strategy for solving the issue of water and nutrient losses from agricultural areas cannot be effective. The same work presented in this paper itself demonstrates the complexity of the issue and how nutrient losses may change depending on several factors, such as soil variability, soil and crop management, nutrient management, farm irrigation system, irrigation water management, presence and depth of groundwater, presence of a drainage network and their interactions. In a given physical system, management has a crucial role; the results of this work showed that, under bad irrigation management, some soils may generate surface water pollution and groundwater even in the case of drip irrigation.

Unfortunately, understanding the role of each of these variables and their interactions, in view of a better management, requires complex and expensive monitoring networks, which is obviously unfeasible at the large scale. However, there are now available modelling tools enabling us to quantitatively predict the effects of different management (of soil, water, nutrients, crop and irrigation systems) under different physical contexts (in terms of climate, soils, depth to water table and water table time evolution). And yet, these models should be handled carefully, as they may

produce completely different predictions depending on the physical system assumed in the simulations. This is why monitoring and modelling should never be seen as alternatives. Actually, models may be of real help in interpreting agricultural pollutant and water fluxes to groundwater and surface drainage network only with a preliminary knowledge of the physical system to be simulated. This is especially true for the bottom-boundary condition. In the case of a shallow groundwater, as in the case considered in this paper, the bottom-boundary may condition significantly the fluxes predicted by the models. That's why, in this paper, knowing the evolution of the depth to water table by using piezometers and tensiometers (see Figure 5) was essential to correctly model the water and solute balance in the soil profile and thus the water and solute fluxes to the runoff and then to the surface drainage network.

This paper also suggests the importance of monitoring and modelling discharges and concentrations along the drainage channels, as these provide an integrated response of relatively large areas and smoothens the effects of soil variability and soil, water and crop management, which is really impossible to monitor at large scale. In this sense, we believe the coupling of a routing model to the agrohydrological model can be an additional strength of the modelling approach we used to analyse the composite dataset observed in this work. In this sense, a routing model calibration based on channel measurements, possibly carried out in different sites along the drainage network, may provide a tool to indirectly validate the goodness of the agrohydrological model simulations. It is worth to recall here that, in this work, the hydraulic parameters used in FLOWS for the different layers in the soil profiles considered were those coming from the initial hydraulic characterization, without any additional calibration. The only calibration concerned the Manning resistance parameter for the elementary fields (n_f=0.030), the ditches (n_f=0.025) and the secondary drainage channel (n_f=0.020) (see Table 3).

When appropriately calibrated, the agrohydrological model may then be used for analysing different alternative management scenarios. Using FLOWS with the appropriate parameterization and top- and bottom-boundary conditions, to optimize irrigation volumes and time of interventions, drastically reduced the water and nutrient losses to the surface drainage network (data not shown here for the sake of brevity). Similarly, in a recent paper, Hassan et al. (2023) demonstrated that optimizing the irrigation volumes and scheduling by using the FLOWS model at irrigation district scale would drastically reduce the losses of water and nutrients to the groundwater compared to the irrigation actually provided by the farmers in an irrigation district of the Apulia Region (Italy).

When adequately calibrated, these models are also the basis for designing technologies for nutrient removals form both groundwater and surface water bodies. Technological tools are available, which have already demonstrated their practical effectiveness (Christianson et al. 2021) and that can be used to prevent nutrient release to water bodies. They may be technologies such as bioreactors and artificial/constructed wetlands, which are simple, relatively low cost and passive treatment systems for removing nitrate and phosphorus (and even pesticides) from both surface water runoff and shallow groundwater systems. However, their effective application requires a prediction of nutrient fluxes to be treated, which can only come from reliable agrohydrological simulations of the system under study.

Improved soil, water and crop management on one side and technologies to remove nutrients from surface and deep percolation fluxes on the other should work in a virtuous sequence where they first look for minimizing the pollutant loads to be treated by pollutant-prevention technologies. To do that, modelling approaches like that used in this paper are essential, as they may help to identify the best management options of water and agrochemicals (timing, quantities and application splitting), as well as agronomic practices (tillage, crop rotations and organic matter content) to minimize the pollutant mass in water leaving agricultural fields and flowing to the surface and groundwater bodies, while still maintaining profitable farmer activities.

Author Contributions

Conceptualization: Antonio Coppola, Shawkat B.M. Hassan. Methodology: Antonio Coppola, Shawkat B.M. Hassan. Software: Antonio Coppola. Investigation: Giovanna Dragonetti, Marco Satta, Silvia Baralla, Myriam Ruberto. Data curation: Giovanna Dragonetti, Marco Satta. Visualization: Giovanna Dragonetti, Marco Satta. Formal analysis: Antonio Coppola, Shawkat B.M. Hassan. Validation: Antonio Coppola, Shawkat B.M. Hassan, Alessandro Comegna. Resources: Raffaella Zucaro, Silvia Baralla, Myriam Rubert, Writing – original draft preparation: Antonio Coppola. Writing – review and editing: Antonio Coppola, Shawkat B.M. Hassan. Funding acquisition: Raffaella Zucaro, Silvia Baralla, Myriam Ruberto. Supervision: Antonio Coppola, Alessandro Comegna. Project administration: Raffaella Zucaro, Silvia Baralla, Myriam Ruberto.

Acknowledgements

Project ARS01_00825 titled 'WATER4AGRIFOOD—Improvement of Mediterranean agri-food productions in conditions of water shortage' is funded by the National Operational Program 'Research and Innovation' 2014–2020 (PON 'R&I' 2014–2020). Open access publishing facilitated by Universita degli Studi della Basilicata, as part of the Wiley - CRUI-CARE agreement.

Data Availability Statement

The data that support the findings of this study are available on request from the corresponding author. The data are not publicly available due to privacy or ethical restrictions.

References

Abbasi, F., J. Simunek, M. T. van Genuchten, et al. 2003. "Overland Water Flow and Solute Transport: Model Development and Field-Data Analysis." *Journal of Irrigation and Drainage Engineering* 129, no. 2: 71–81. https://doi.org/10.1061/(ASCE)0733-9437(2003)129:2(71).

Allen, R. G., Pereira, L. S., Raes, D., & Smith, M. (1998). "Guidelines for Computing Crop Water Requirements." Irrigation and Drainage Paper 56.

Barrow, N. J., L. Madrid, and A. M. Posner. 1981. "A Partial Model for the Rate of Adsorption and Desorption of Phosphate by Goethite." *Journal of Soil Science* 32: 399–407.

Cabon, F., G. Girard, and E. Ledoux. 1991. "Modelling of the Nitrogen Cycle in Farm Land Areas." *Fertilizer Research* 27, no. 2: 161–169. https://doi.org/10.1007/BF01051124.

Childs, E. C., and N. Collis-George. 1997. "The Permeability of Porous Materials." *Proceedings of the Royal Society of London. Series A.*

Mathematical and Physical Sciences 201, no. 1066: 392–405. https://doi.org/10.1098/rspa.1950.0068.

Christianson, L. E., R. A. Cooke, C. H. Hay, et al. 2021. "Effectiveness of Denitrifying Bioreactors on Water Pollutant Reduction From Agricultural Areas." *Transactions of the ASABE* 64, no. 2: 641–658. https://doi.org/10.13031/trans.14011.

Cleveland, C. C., and D. Liptzin. 2007. "C:N:P Stoichiometry in Soil: Is There a "Redfield Ratio" for the Microbial Biomass?" *Biogeochemistry* 85, no. 3: 235–252. https://doi.org/10.1007/s10533-007-9132-0.

Coppola, A. 2000. "Unimodal and Bimodal Descriptions of Hydraulic Properties for Aggregated Soils." *Soil Science Society of America Journal* 64, no. 4: 1252–1262. https://doi.org/10.2136/sssaj2000.6441252x.

Coppola, A., M. Abdallah, G. Dragonetti, P. Zdruli, and N. Lamaddalena. 2019a. "Monitoring and Modelling the Hydrological Behaviour of a Reclaimed Wadi Basin in Egypt." *Ecohydrology* 12, no. 4: e2084. https://doi.org/10.1002/eco.2084.

Coppola, A., A. Basile, X. Wang, et al. 2011. "Hydrological Behaviour of Microbiotic Crusts on Sand Dunes: Example From NW China Comparing Infiltration in Crusted and Crust-Removed Soil." *Soil and Tillage Research* 117: 34–43. https://doi.org/10.1016/j.still.2011.08.003.

Coppola, A., N. Chaali, G. Dragonetti, N. Lamaddalena, and A. Comegna. 2015. "Root Uptake Under Non-uniform Root-Zone Salinity." *Ecohydrology* 8, no. 7: 1363–1379. https://doi.org/10.1002/eco.1594.

Coppola, A., G. Dragonetti, A. Comegna, et al. 2014. "Mapping Solute Deep Percolation Fluxes at Regional Scale by Integrating a Process-Based Vadose Zone Model in a Monte Carlo Approach." *Soil Science and Plant Nutrition* 60, no. 1: 71–91. https://doi.org/10.1080/00380768.2013.855615.

Coppola, A., G. Dragonetti, A. Sengouga, et al. 2019b. "Identifying Optimal Irrigation Water Needs at District Scale by Using a Physically Based Agro-Hydrological Model." *Water* 11, no. 4: 841. https://doi.org/10.3390/w11040841.

Coppola, A., H. H. Gerke, A. Comegna, A. Basile, and V. Comegna. 2012. "Dual-Permeability Model for Flow in Shrinking Soil With Dominant Horizontal Deformation." *Water Resources Research* 48, no. 8: W08527. https://doi.org/10.1029/2011WR011376.

Coppola, A., K. Smettem, A. Ajeel, et al. 2016. "Calibration of an Electromagnetic Induction Sensor With Time-Domain Reflectometry Data to Monitor Rootzone Electrical Conductivity Under Saline Water Irrigation." *European Journal of Soil Science* 67, no. 6: 737–748. https://doi.org/10.1111/ejss.12390.

Durner, W. 1994. "Hydraulic Conductivity Estimation for Soils With Heterogeneous Pore Structure." *Water Resources Research* 30, no. 2: 211–223. https://doi.org/10.1029/93WR02676.

European Commission. 2021. "Report From the Commission to the Council and the European Parliament on the Implementation of Council Directive 91/676/EEC Concerning the Protection of Waters Against Pollution Caused by Nitrates From Agricultural Sources Based on Member State Reports for the Period 2016–2019." Brussels, 11-10-2021.

Feddes, R. A., P. J. Kowalik, and H. Zaradny. 1978. *Simulation of Field Water Use and Crop Yield*. Wageningen, The Netherlands: Centre for Agricultural Publishing and Documentation.

Feddes, R. A., and P. A. C. Raats. 2004. "Parameterizing the Soil-Water-Plant Root System." In *Unsaturated-Zone Modeling: Progress, Challenges, Applications*, edited by R. A. Feddes et al., vol. 6. Wageningen UR Frontis Series, 95–141. Wageningen, The Netherlands: Kluwer Academic Press.

Fischer, H., E. List, R. Koh, J. Imberger, and N. Brooks. 1979. *Mixing in Inland and Coastal Waters*. San Diego, California: Academic Press.

Gardner, W. R. 1958. "Some Steady-State Solutions of the Unsaturated Moisture Flow Equation With Applications to Evaporation From a Water Table." *Soil Science* 85: 228–232.

Ghiglieri, G., A. Carletti, S. Da Pelo, et al. 2016. "Three-Dimensional Hydrogeological Reconstruction Based on Geological Depositional Model: A Case Study From the Coastal Plain of Arborea (Sardinia, Italy)." *Engineering Geology* 207: 103–114. https://doi.org/10.1016/j.enggeo.2016.04.014.

Hansen, S., P. Abrahamsen, C. T. Petersen, and M. Styczen. 2012. "Daisy: Model Use, Calibration and Validation." *Transactions of the ASABE* 55, no. 4: 1315–1333.

Hassan, S. B. M., G. Dragonetti, A. Comegna, N. Lamaddalena, and A. Coppola. 2023. "Analyzing the Role of Soil and Vegetation Spatial Variability in Modelling Hydrological Processes for Irrigation Optimization at Large Scale." *Irrigation Science* 42: 249–267. https://doi.org/10.1007/s00271-023-00882-7.

Hassan, S. B. M., G. Dragonetti, A. Comegna, A. Sengouga, N. Lamaddalena, and A. Coppola. 2022. "A Bimodal Extension of the ARYA&PARIS Approach for Predicting Hydraulic Properties of Structured Soils." *Journal of Hydrology* 610: 127980. https://doi.org/10.1016/j.jhydrol.2022.127980.

Hooghoudt, S. B. 1940. *General Consideration of the Problem of Field Drainage by Parallel Drains, Ditches, Watercourses, and Channels*. Vol. 7. Contribution to the Knowledge of Some Physical Parameters of the Soil [In Dutch.]. Groningen, The Netherlands: Bodemkundig Instituut.

Jaynes, D. B., and T. M. Isenhart. 2014. "Reconnecting Tile Drainage to Riparian Buffer Hydrology for Enhanced Nitrate Removal." *Journal of Environmental Quality* 43, no. 2: 631–638. https://doi.org/10.2134/jeq2013.08.0331.

Kelleners, T. J., G. B. Paige, and S. T. Gray. 2009. "Measurement of the Dielectric Properties of Wyoming Soils Using Electromagnetic Sensors." *Soil Science Society of America Journal* 73, no. 5: 1626–1637. https://doi.org/10.2136/sssaj2008.0361.

Klute, A., and C. Dirksen. 1986. "Hydraulic Conductivity and Diffusivity: Laboratory Methods." In *Methods of Soil Analysis*, edited by A. Klute, 687–734. Madison, WI: American Society of Agronomy, Soil Science Society of America. https://doi.org/10.2136/sssabookser5.1.2ed.c28.

Lafolie, F. 1991. "Modelling Water Flow, Nitrogen Transport and Root Uptake Including Physical Non-Equilibrium and Optimization of the Root Water Potential." *Fertilizer Research* 27, no. 2: 215–231. https://doi.org/10.1007/BF01051129.

Liang, X. Q., Y. X. Chen, H. Li, et al. 2007. "Modeling Transport and Fate of Nitrogen From Urea Applied to a Near-Trench Paddy Field." *Environmental Pollution* 150, no. 3: 313–320.

Luckner, L., M. T. Van Genuchten, and D. R. Nielsen. 1989. "A Consistent Set of Parametric Models for the Two-Phase Flow of Immiscible Fluids in the Subsurface." *Water Resources Research* 25, no. 10: 2187–2193. https://doi.org/10.1029/WR025i010p02187.

Maas, E. V., and G. J. Hoffman. 1977. "Crop Salt Tolerance-Current Assessment." *Journal of the Irrigation and Drainage Division* 103, no. 2: 115–134.

Mansell, R. S., H. M. Selim, and J. G. A. Fiskell. 1977. "Simulated Transformations and Transport of Phosphorus in Soil." *Soil Science* 124, no. 2: 102–109.

Mansell, R. S., H. M. Selim, P. Kanchanasut, J. M. Davidson, and J. G. A. Fiskell. 1977. "Experimental and Simulated Transport of Phosphorus Through Sandy Soils." *Water Resources Research* 13, no. 1: 189–194. https://doi.org/10.1029/WR013i001p00189.

McGechan, M. B., and L. Wu. 2001. "A Review of Carbon and Nitrogen Processes in European Soil Nitrogen Dynamics Models." In *Modelling Carbon and Nitrogen Dynamics for Soil Management*, edited by M. J. Shaffer, L. Ma, and S. Hansen, 103–171. Boca Raton, FL: Lewis Publishers.

Mollerup, M., P. Abrahamsen, C. T. Petersen, and S. Hansen. 2014. "Comparison of Simulated Water, Nitrate, and Bromide Transport Using a Hooghoudt-Based and a Dynamic Drainage Model." *Water Resources Research* 50: 1080–1094. https://doi.org/10.1002/2012WR013318.

Mualem, Y. 1976. "A New Model for Predicting the Hydraulic Conductivity of Unsaturated Porous Media." *Water Resources Research* 12, no. 3: 513–522. https://doi.org/10.1029/WR012i003p00513.

Nguyen, T. P. L., G. Seddaiu, and P. P. Roggero. 2014. "Hybrid Knowledge for Understanding Complex Agri-Environmental Issues: Nitrate Pollution in Italy." *International Journal of Agricultural Sustainability* 12, no. 2: 164–182. https://doi.org/10.1080/14735903.2013.825995.

Prasad, R. 1988. "A Linear Root Water Uptake Model." *Journal of Hydrology* 99, no. 3: 297–306.

Ritchie, J. T. 1972. "Model for Predicting Evaporation From a Row Crop With Incomplete Cover." *Water Resources Research* 8, no. 5: 1204–1213. https://doi.org/10.1029/WR008i005p01204.

Ross, P. J., and R. J. Smettem. 1993. "Describing Soil Hydraulic Properties With Sums of Simple Functions." *Soil Science Society of America Journal* 57: 26–29.

Russo, D. 1988. "Determining Soil Hydraulic Properties by Parameter Estimation: On the Selection of a Model for the Hydraulic Properties." *Water Resources Research* 24, no. 3: 453–459.

Scotter, D. R., and P. J. Ross. 1994. "The Upper Limit of Solute Dispersion and Soil Hydraulic Properties." *Soil Science Society of America Journal* 58, no. 3: 659–663. https://doi.org/10.2136/sssaj1994.03615995005800030004x.

Shi, J., Q. Zuo, and R. Zhang. 2007. "An Inverse Method to Estimate the Source-Sink Term in the Nitrate Transport Equation." *Soil Science Society of America Journal* 71, no. 1: 26–34. https://doi.org/10.2136/sssaj2005.0395.

Singh, V. P., and V. Aravamuthan. 1996. "Errors of Kinematic-Wave and Diffusion-Wave Approximations for Steady-State Overland Flows." *Catena* 27, no. 3: 209–227. https://doi.org/10.1016/0341-8162(96)00021-5.

Topp, G. C., J. L. Davis, and A. P. Annan. 1980. "Electromagnetic Determination of Soil Water Content: Measurements in Coaxial Transmission Lines." *Water Resources Research* 16, no. 3: 574–582. https://doi.org/10.1029/WR016i003p00574.

Van Dam, J. C., J. Huygen, J. G. Wesseling, et al. 1997. *Theory of SWAP Version 2.0; Simulation of Water Flow, Solute Transport and Plant Growth in the Soil-Water-Atmosphere-Plant Environment*. Wageningen, The Netherlands: DLO Winand Staring Centre.

van der Molen, W. H., and J. Wesseling. 1991. "A Solution in Closed Form and a Series Solution to Replace the Tables for the Thickness of the Equivalent Layer in Hooghoudt's Drain Spacing Formula." *Agricultural Water Management* 19, no. 1: 1–16. https://doi.org/10.1016/0378-3774(91)90058-Q.

Van Der Zee, S. E., and W. H. Van Riemsdijk. 1986. "Sorption Kinetics and Transport of Phosphate in Sandy Soil." *Geoderma* 38, no. 1: 293–309. https://doi.org/10.1016/0016-7061(86)90022-4.

van Genuchten, M. T. 1980. "A Closed-Form Equation for Predicting the Hydraulic Conductivity of Unsaturated Soils." *Soil Science Society of America Journal* 44, no. 5: 892–898. https://doi.org/10.2136/sssaj1980.03615995004400050002x.

van Genuchten, M. T., and G. J. Hoffman. 1984. "Analysis of Crop Salt Tolerance Data." In *Soil Salinity Under Irrigation – Process and Management*, edited by I. Shainberg and J. Shalhevet, vol. 51, 258–271. New York: Springer. Ecological Studies.

van Genuchten, M. T., and R. Nielsen. 1985. "On Describing and Predicting the Hydraulic Properties." *Annales Geophysicae* 3, no. 5: 615–628.

van Venuchten, M. T. 1987. *A Numerical Model for Water and Solute Movement in and Below the Root Zone*. Riverside: USDA-ARS, US Salinity Laboratory Research Report No. 121.

Vrugt, J. A., J. W. Hopmans, and J. Šimunek. 2001. "Calibration of a Two-Dimensional Root Water Uptake Model." *Soil Science Society of America Journal* 65, no. 4: 1027–1037.

Wallach, R., and M. T. van Genuchten. 1990. "A Physically Based Model for Predicting Solute Transfer From Soil Solution to Rainfall-Induced Runoff Water." *Water Resources Research* 26, no. 9: 2119–2126. https://doi.org/10.1029/WR026i009p02119.

Woolhiser, D. A. 1975. "The Watershed Approach to Understanding Our Environment." *Journal of Environmental Quality* 4, no. 1: 17–21. https://doi.org/10.2134/jeq1975.00472425000400010003x.

Appendix A

FLOWS Agrohydrological Model

FLOWS (FLOws of Water and Solutes in soils) is a dynamic physically based model to simulate water flow and solute transport in the soil–plant–atmosphere system. The numerical code, written in Matlab, solves the 1D form of the Richards equation (RE) for water flow and the 1D advection–dispersion equation (ADE) for solute transport. Heat flow is also simulated in the model since several parameters related to nutrient reactions and transport and various partitioning and production coefficients are strongly temperature dependent.

As for water flow, the model allows us to set several top- and bottom-boundary conditions, both constant and variable over time: potential and fluxes at the top boundary and potential, fluxes and hydraulic gradient at the bottom boundary. Initial conditions may be given as pressure heads, which can be either constant along the soil profile or variable node by node.

As for solute transport, the model allows for either constant or variable solute application at the soil surface. Also, initial conditions may be either constant or variable node by node. Dispersivity and decay may also be given for each node.

Figure A1 summarizes the processes that can be simulated by FLOWS. For agricultural–environmental management purposes, FLOWS enables the integrated simulation of chemical transformations and transport of organic and inorganic carbon, nitrogen and phosphorus simultaneously (in the same discretization time step) with the simulation of water contents and related flows. It also allows irrigation management, optimizing irrigation times and volumes according to a criterion based on the average water potential in the root zone. FLOWS also simulates the flows of water and nutrients towards artificial drainage and surface runoff. Furthermore, the model offers the possibility to carry out multisite simulations, which can be particularly important for spatially distributed simulations, as well as for simulations performed in a stochastic environment (e.g., Monte Carlo). In the following, we provide a more detailed description of the main code modules used in this paper.

A.1 | Water Flow

FLOWS simulates water flow by solving the RE using an implicit pressure-based, finite-difference scheme with explicit linearization (Van Dam et al. 1997):

$$C(h)\frac{\partial h}{\partial t} = \frac{\partial}{\partial z}\left(K(h)\frac{\partial h}{\partial z} + K(h)\right) - S_w \qquad \text{(A1)}$$

where $C(h) = d\theta/dh$ (L^{-1}) is the soil water capacity, h (L) is the soil water pressure head, t (T) is time, z (L) is the vertical coordinate being positive upward, $K(h)$ (LT^{-1}) is the hydraulic conductivity and S_w (T^{-1}) is a sink term describing water uptake by plant roots, S_r, and/or lateral water drainage, S_{dr}, so that $S_w = S_r + S_{dr}$.

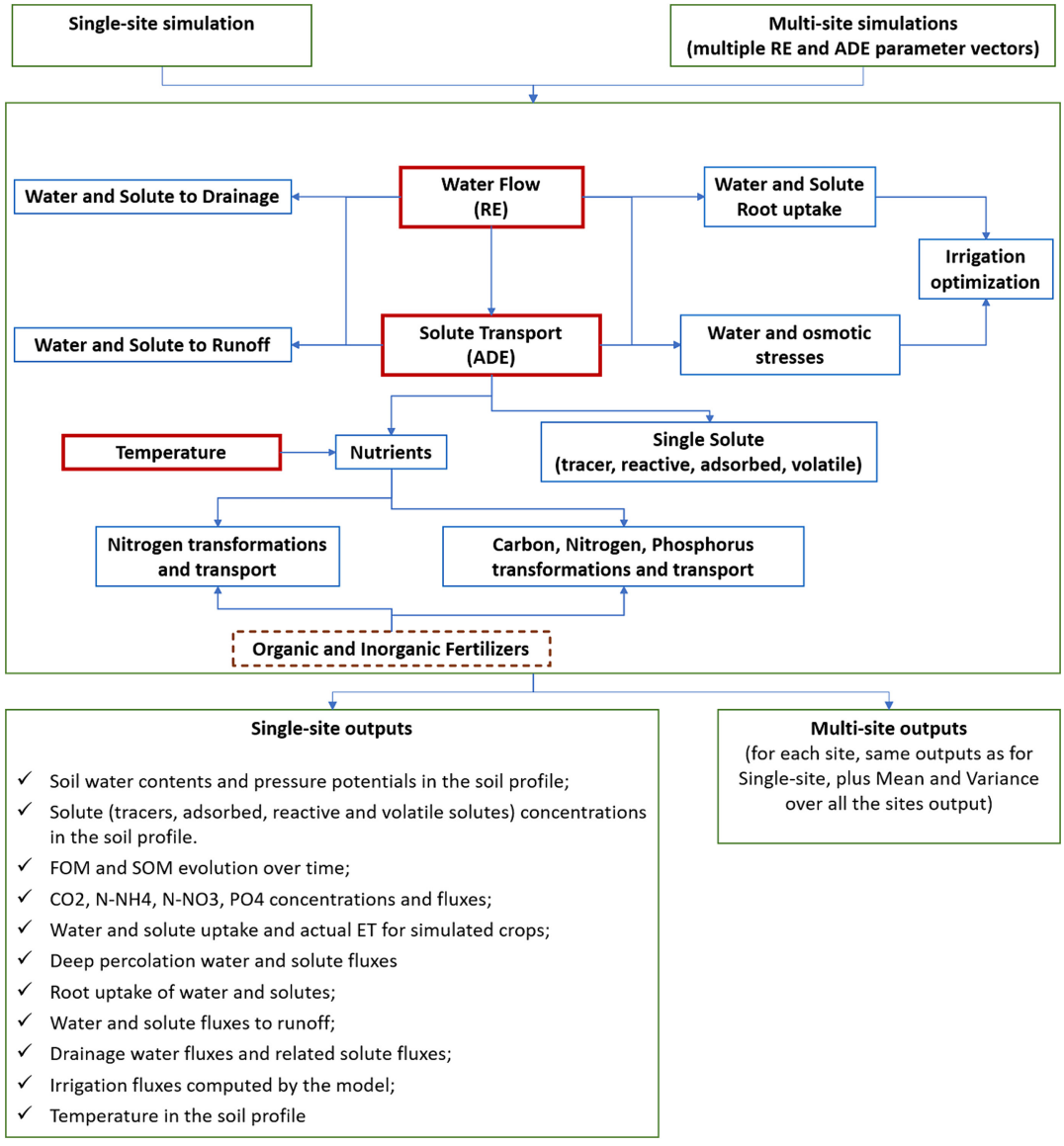

FIGURE A1 | Schematic representation of all processes simulated in FLOWS, their interactions and simulation options. The model provides all outputs listed in the box at the bottom. In the box, FOM and SOM stand for fresh organic matter and stable organic matter (humus), respectively. In the case of multiple simulations (e.g., spatially distributed simulations or iterated simulations in stochastic frameworks), all outputs are provided for each of the input parameter vectors, together with the mean and variance of each output.

To be solved, Equation (A1) requires the water retention, $\theta(h)$, and the hydraulic conductivity, $K(h)$, functions to be known. FLOWS allows opting for several hydraulic property models: (1) unimodal van Genuchten–Mualem model (Mualem 1976; van Genuchten 1980); (2) bimodal Durner–Mualem model (Durner 1994); (3) bimodal Ross and Smettem–Mualem model (Ross and Smettem 1993); and (4) unimodal Russo–Gardner model (Gardner 1958; Russo 1988).

A.2 | Root Water Sink Term, S_r, and Actual Transpiration, T_a

In FLOWS, the crop is simulated in a so-called static way, so that the crop growth is not simulated dynamically by the model, but the user has to specify the crop development stage by giving as input the evolution over time of the leaf area index, LAI; root depth, D_r; reference evapotranspiration, ET_r; as well as the crop coefficient, Kc, as a function of the development stage to convert reference evapotranspiration to the potential evapotranspiration, ET_p, of the considered crop.

The root water uptake term, S_r, is computed in FLOWS using a macroscopic approach commonly employed in hydrological soil–plant–atmosphere continuum models for describing plant water uptake (Feddes, Kowalik, and Zaradny 1978; Feddes and Raats 2004). First, the potential transpiration, T_p, is distributed over the root depth according to a root density distribution function, $g(z)$, selected by the user, thus giving the potential root sink term, $S_{r,p}$, at any simulation depth node. FLOWS allows selecting different alternative root distributions: (1) uniform (Feddes, Kowalik, and Zaradny 1978); (2) triangular (Prasad) (Prasad 1988); (3) Vrugt (Vrugt, Hopmans, and Šimunek 2001); or (4) logistic.

Within the macroscopic approach, the potential sink term is converted to the actual sink term, S_r, through the introduction of an uptake reduction function, $\alpha(h,h_{os})$, accounting for the possible water stress (related to soil water potential, h) and osmotic stress (related to the osmotic potential, h_{os}) experienced by roots at different depths within the root zone. FLOWS allows selecting different alternative reduction function accounting for water uptake reduction: (1) Feddes reduction function for water stress (Feddes and Raats 2004); (2) van Genuchten reduction function for water stress (van Genuchten 1987); (3) Maas and Hoffman reduction function for osmotic stress (Maas and Hoffman 1977); (4) van Genuchten reduction function for osmotic stress (van Genuchten and Hoffman 1984); (5) multiplicative combinations of water and osmotic reduction function as described above.

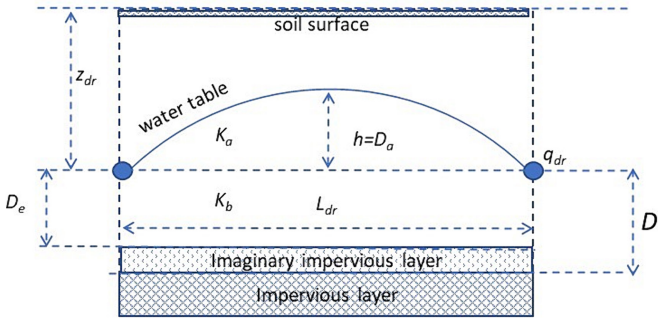

FIGURE A2 | Schematic view of the artificial drains as well as the parameters and system involved in Hooghoudt's equation.

Thus, the actual root uptake sink term is obtained as $\alpha(h,h_{os})\, S_{r,p}$.

A.3 | Artificial Drainage Sink Term, S_{dr}

The other component of S_w, the fluxes to artificial drainage, S_{dr}, is modelled based on the Hooghoudt theory (Hooghoudt 1940) for lateral flow towards drains (Figure A2). Previous studies have shown that employing a 1D solution to the flow system, coupled with the Hooghoudt theory, yields comparable outcomes to a 2D solution that explicitly represents drain tiles, provided that an appropriate implementation of the Hooghoudt theory is used. This matter has been thoroughly investigated by Mollerup et al. (2014).

Whenever the water table is positioned above either a drainpipe or an open-field drain, water will naturally flow towards the drain. Hooghoudt (1940) provides a method to calculate the steady-state drain flux per unit surface area, denoted as q_{dr}, which is expressed as follows:

$$q_{dr} = \frac{8K_b D_{eq} D_a + 4K_a D_a^2}{L_{dr}^2} \tag{A2}$$

In this equation, K_a represents the hydraulic conductivity of the saturated layer located above the drain level, while K_b represents the hydraulic conductivity of the layer positioned below the drain level. The parameter L_{dr} is the distance between the drains. Additionally, the water table height above the drain at $0.5L_{dr}$ is denoted as D_a, which corresponds to the variable 'h' in Hooghoudt's work.

D_{eq} represents the equivalent drain depth, influenced by both the vertical separation between the drains and the impermeable layer (D_{imp}) as well as the hydraulic radius of the drain (R_{dr}). When the drain pipe or open drains do not extend to the impermeable layer, D_{eq} is substituted for D_{imp}. The Hooghoudt theory, which governs lateral flow to drains, operates on the premise of horizontal flow lines, in alignment with the Dupuit–Forchheimer theory. However, if drains are situated above the impermeable layer, the flow lines will converge towards the drain (radial flow lines), deviating from horizontal orientation. Consequently, these elongated flow lines necessitate additional head loss to maintain consistent water volume flow into the drains, resulting in a raised water table. In order to preserve the notion of horizontal flow, Hooghoudt (1940) posited an imaginary impermeable layer above the actual one, thereby reducing the thickness of the layer through which water travels towards the drains. To compute D_{imp}, van der Molen and Wesseling (1991) presented an analytical solution:

$$\begin{aligned} D_{eq} &= \frac{1}{8}\frac{\pi L_{dr}}{ln\left(\frac{L_{dr}}{\pi R_{dr}}\right)+F(x)} \\ x &= \frac{2\pi D_{imp}}{L_{dr}} \\ F(x) &= \frac{\pi^2}{4x} + ln\left(\frac{x}{2\pi}\right) \qquad \text{for } x<0.5 \\ F(x) &= \sum_{i=1}^{\infty} \frac{4e^{(-4i+2)x}}{(2i-1)\left(1-e^{(-4i+2)x}\right)} \qquad \text{for } x\geq 0.5 \end{aligned} \tag{A3}$$

For x values less than 0.5, the function $F(x)$ converges quickly, while for x values greater than 1, it exhibits rapid convergence. As outlined in the methodology introduced by Mollerup et al. (2014), the FLOWS model determines S_{dr} by initially segmenting q_{dr} into two constituents: q_a, originating from above the drain level, and q_b, originating from below the drain level:

$$\begin{aligned} q_a &= \frac{4K_a D_a^2}{L_{dr}^2} \\ q_b &= \frac{8K_b D_{eq} D_a}{L_{dr}^2} \end{aligned} \tag{A4}$$

In FLOWS, K_a and K_b are comparted-weighted averages representing the saturated nodes above and below the drain level, respectively, following the approach adopted in the Daisy model (Hansen et al. 2012):

$$\begin{aligned} K_a &= \frac{\sum_i \xi \Delta z_i K_{0,i}}{D_a}, \\ D_a &= \sum_i \xi \Delta z_i \quad \text{for all the nodes } i \text{ above the drain level} \\ K_b &= \frac{\sum_i \xi \Delta z_i K_{0,i}}{D_b}, \\ D_b &= \sum_i \xi \Delta z_i \quad \text{for all the nodes } i \text{ below the drain level} \end{aligned} \tag{A5}$$

When $\xi=1$, it indicates saturated nodes, while $\xi=0$ corresponds to unsaturated nodes, which do not contribute to the flow to drains. Here, Δz_i represents the thickness of each simulation node compartment. The weighted average is essential as it accommodates the likelihood that the layer above (and below) the drain may encompass nodes with various saturated hydraulic conductivities. If $K_{0,i}$ remains consistent across all nodes in the layer above the drain (forming a homogeneous layer), then K_a would equate to $K_{0,i}$. The same principle applies to the layer situated below the drain level.

Ultimately, the S_{dr} for each of the N simulation nodes is determined by distributing the fluxes q_a and q_a across the saturated nodes positioned both above and below the drain level:

$$\begin{aligned} S_{dr,a} &= \frac{\xi K_{0,i}}{K_a D_a} q_a \qquad \text{for all the nodes } i \text{ above the drain level} \\ S_{dr,b} &= \frac{\xi K_{0,i}}{K_b D_b} q_b \qquad \text{for all the nodes } i \text{ below the drain level} \\ S_{dr} &= S_{dr,a} + S_{dr,b} \end{aligned} \tag{A6}$$

A.4 | Water to Runoff

FLOWS simulate the occurrence of runoff under two conditions: first, when the intensity of rainfall overcomes the soil surface's infiltration capacity (referred to as the Hortonian mechanism of runoff) and, second, when the soil profile becomes completely saturated (referred to as the

Dunnian mechanism of runoff). The first condition (Hortonian) is defined by a calculating the maximum infiltration velocity at the soil surface, fs_{max}:

$$fs_{max} = K_{m,max}\left(\frac{h_1 - h_{surf,max}}{\Delta z_{top}} - 1\right) \quad (A7)$$

where $K_{m,max}$ is the arithmetic average between the surface and top node hydraulic conductivities, h_1 is the pressure head at the top node, $h_{surf,max}$ is the maximum pressure head allowed at the surface (generally, $h_{surf,max} = 0$) and Δz_{top} is the depth of the top node.

If the incoming fluxes (e.g., precipitation and/or irrigation), q_{surf}, exceeds fs_{max}, the model changes the top-boundary condition to a pressure head boundary condition by imposing the top-boundary pressure head $h_{top} = h_{surf,max}$. In case abs(q_{surf}) > K_0 for the first node, the value of ($q_{surf} - fs_{max}$) becomes runoff.

Regarding the Dunnian runoff mechanism, during each time step (Δt), the model computes the total saturation storage and the current storage across the entire simulation domain. If the difference in storage ($\Delta\theta_s - \Delta\theta$) is less than or equal to a predefined tolerance (ε), all incoming flux (q_{surf}) during that time step (Δt) will be calculated as runoff.

A.5 | Solute Transport

As for solute transport, FLOWS solves the ADE by an explicit, central difference scheme, which, compared to an implicit iterative scheme, allows for a relatively easy inclusion of non-linear adsorption and other non-linear processes simulated in the code:

$$\frac{\partial\theta C}{\partial t} + \rho_b\frac{\partial C_s}{\partial t} + \frac{\partial\theta_g C_g}{\partial t} = -\frac{\partial qC}{\partial z} + \frac{\partial}{\partial z}\left(\theta D_h\frac{\partial C}{\partial z}\right) + \frac{\partial}{\partial z}\left(\theta_g D_g^s K_H\frac{\partial C}{\partial z}\right) - S_s \quad (A8)$$

Equation (A8) includes linear and non-linear adsorption, linear volatilization, linear decay and proportional root uptake in unsaturated/saturated soil. In the equation, C (M L^{-3}), C_s (M M^{-1}) and C_g (M L^{-3}), are the amount of solute in the liquid, adsorbed and gaseous phases, respectively; q (L T^{-1}) is the Darcian water flux; ρ_b (M L^{-3}) is the bulk density; D_h (L^2 T^{-1}) is the hydrodynamic dispersion coefficient; $D_g^s$is the dispersion coefficient in the gaseous phases (L^2 T^{-1}); θ_g is the volumetric air content in soil; S_s (ML^{-3}T^{-1}) is a source–sink term for solutes, K_H is the dimensionless Henry constant. Hydrodynamic dispersion is related to the molecular diffusion constant of the solute in bulk water, D_0 (L^2 T^{-1}), and the average pore water velocity, $v = q/\theta$, as follows:

$$D_h = \lambda v + \eta(\theta)D_0 \quad (A9)$$

where λ (L) is the dispersivity and η is a tortuosity coefficient.

As for sorption, the model allows for both linear and Freundlich isotherms.

A.6 | Solute Transfer to Artificial Drainage and Runoff

The solute flux to drainage is calculated in FLOWS by simply multiplying the drainage sink term, S_{dr} by the solute concentration, C, at the same simulation node.

As for the solute transfer from the soil solution to runoff, FLOWS calculates the solute flux, q_s (g/cm^2/day), across the soil surface interface as a function of the difference in concentration between the soil solution at the top boundary, $C(0,t)$ and runoff water (C_{run}), multiplied by a mass transfer coefficient, denoted as k_{run} (cm/day) (Wallach and van Genuchten 1990):

$$q_s(0,t) = -\theta D_h\frac{\partial C}{\partial z} + v\theta C\Big|_{z=0} = \left(-\theta k_{run}\left[C(0,t) - C_{run}\right]\right) \quad (A10)$$

Equation (A10) incorporates both convective and dispersive transfers between the soil and runoff water. Convective mass transport is oriented downward, while diffusive–dispersive transport is oriented upward. The value of k_{run} is primarily determined by the diffusion coefficient, but it can also be affected by various flow characteristics such as runoff water depth, rainfall intensity and duration, as well as surface roughness. By assuming that the value of C_{run} can be neglected, Equation (A10) becomes

$$-D_h\frac{\partial C}{\partial z} + (v + k_{run})C\Big|_{z=0} = 0 \quad (A11)$$

applying for finite values of k_{run}, from which the flux to runoff may be calculated.

A.7 | Transformations and Transport of Nutrients in FLOWS

The FLOWS model manages the addition of fertilizers in various forms such as manure, crop residue and mineral fertilizers. It requires information on the application time and the incorporation depth (referred to as z_{fert} in the FLOWS code) as inputs. The model assumes that fertilizer is uniformly distributed across the incorporation depth. In addition, it also allows for adding solutes (including nutrients) as a time-variable top-boundary condition. In FLOWS, the transformations of carbon, nitrogen and phosphorus are governed by the dynamics of organic matter decomposition and, thus, influenced by the carbon-to-nitrogen (C:N) and carbon-to-phosphorus (C:P) ratios (Cleveland and Liptzin 2007).

Nitrogen in the form of N-NH_4 and N-NO_3, as well as phosphorus in the form of P-PO_4, originating from organic mineralization, joins the mineral pools of N-NH_4 and N-NO_3 and P-PO_4. This is supplemented by inputs from mineral fertilizers, such as urea ($UREA_{FRT}$) for nitrogen, and solid and liquid NH_4 and NO_3 fertilizers ($S\&L\_NH4_{FERT}$ and $S\&L\_NO3_{FERT}$, respectively), along with solid and liquid PO_4 fertilizers ($S\&L\_PO4_{FERT}$) for phosphorus.

The subsequent transformations of these mineral pools of N-NH_4, N-NO_3 and P-PO_4 are governed by various reaction processes, often characterized as first-order decay, each associated with specific constants.

A.8 | Nitrogen

As for nitrogen, urea undergoes hydrolysis following a first-order decay with a constant k_{hyd}, resulting in the production of NH_4, and a portion of this NH_4 volatilizes, governed by a decay constant k_{vol} (Liang et al. 2007):

$$\begin{aligned} rNH4_{hUR} &= UR_0 K_{hyd}\exp\left(-k_{hyd}t\right) \\ rNH3_{vUR} &= NH4_{hUR} K_{vol}\exp\left(-k_{vol}t\right) \end{aligned} \quad (A12)$$

where $rNH4_{hur}$ is the rate of urea hydrolysis. Hereafter, the prefix r refers to rates. UR_0 is the initial urea concentration and $rNH3_{vUR}$ is the rate of urea volatilization and $NH4_{hur}$ is the ammonium concentration coming from urea hydrolysis.

Nitrification and denitrification can occur to N-NH_4 and N-NO_3 in the soil solution phase. Additionally, N-NH_4 can be adsorbed to the solid soil fraction through a linear isotherm with a distribution coefficient k_{ads}. Furthermore, soil N-NH_4 and N-NO_3 can be taken up by roots or drawn by artificial drains.

Therefore, the concentrations of remaining N-NH_4 and N-NO_3 are transported through the soil via advection–dispersion. Consequently, for nitrogen transport, the ADE is applied twice:

$$\frac{\partial\theta C_{NH}}{\partial t} + \rho_b\frac{\partial C_{a,NH}}{\partial t} = \frac{\partial qC_{NH}}{\partial z} + \frac{\left(\partial\theta D\frac{\partial C_{NH}}{\partial z}\right)}{\partial z} - Ss_{NH} \quad (A13)$$

$$\frac{\partial \theta C_{NO}}{\partial t} + \rho_b \frac{\partial C_{a,NO}}{\partial t} = \frac{\partial q C_{NO}}{\partial z} + \frac{\left(\partial \theta D \frac{\partial C_{NO}}{\partial z}\right)}{\partial z} - Ss_{NO} \quad \text{(A14)}$$

The subscripts NH and NO represent the N-NH_4 and N-NO_3 forms of nitrogen, respectively. It is assumed that both N-NH_4 and N-NO_3 can be adsorbed onto the solid phase, with N-NO_3 being adsorbed on a positively charged surface. It is important to note that these two equations are interconnected through the nitrification process, which converts a portion of N-NH_4 (acting as a sink term in Equation A13) into N-NO_3 (acting as a source in Equation A14).

In Equations (A13) and (A14), Ss_{NH} and Ss_{NO} represent the source–sink terms of solute, which vary with depth (z) and time (t). They can be expressed as follows:

$$\begin{aligned} Ss_{NH} &= -Ss_{minNH} - Ss_{urea} - Ss_{frtNH} + Ss_{nit} + Ss_{vol} + Ss_{upNH} + Ss_{drNH} \\ Ss_{NO} &= -Ss_{nit} - Ss_{frtNO} + Ss_{den} + Ss_{upNO} + Ss_{drNO} \end{aligned} \quad \text{(A15)}$$

Ss_{minNH} and Ss_{urea} represent the N-NH_4 derived from mineralization (which is not included in this study) and urea hydrolysis (as described in Equation A12), respectively. Ss_{nit} denotes the N-NH_4 altered through nitrification. Ss_{den} and Ss_{vol} represent the N-NO_3 and N-NH_4 lost due to denitrification and volatilization, respectively. Ss_{upNH} and Ss_{upNO} indicate the N-NH_4 and N-NO_3 absorbed by roots, respectively. Similarly, Ss_{drNH} and Ss_{drNO} represent the loss of N-NH_4 and N-NO_3 through artificial drainage, respectively. Finally, Ss_{frtNH} and Ss_{frtNO} are the N-NH_4 and N-NO_3 source terms coming from mineral fertilizers additions (other than urea).

The source terms Ss_{minNH}, Ss_{urea}, Ss_{frtNH} and Ss_{frtNO} are derived by dividing the rates of mineralization, urea hydrolysis and mineral fertilizer addition (all expressed in grammes per square centimetre of soil per day) by the incorporation depth, z_{fert} (in centimetres). This yields the corresponding Ss terms (expressed in grammes per cubic centimetre of soil per day), which are then added to each of the calculation nodes within the z_{fert} depth. Table A1 summarizes the equations describing the liquid-phase nitrogen transformations in FLOWS.

In Table A1, UR_0 and UR_{NH4} represent the initial urea concentration and the N-NH_4 produced as a result of urea hydrolysis, respectively. Furthermore, k_{nit} and k_{den} represent the optimal first-order rate coefficients for the processes of nitrification of N-NH_4 and denitrification of N-NO_3, respectively. T stands for the actual soil temperature in degree Celsius, while T_{opt} indicates the optimum temperature for the process in degrees Celsius (Cabon, Girard, and Ledoux 1991). θ_d represents the threshold water content for denitrification.

Additionally, $K_{r,NH}$ and $K_{r,NO}$ denote the root uptake preference factors (dimensionless) for N-NH_4 and N-NO_3, respectively, reflecting positive or negative selection of solute ions relative to the extracted soil water amount (Van Dam et al. 1997). For passive uptake, K_r is set to 1.

S_r and S_{dr} represent the source–sink terms associated with root uptake and artificial drainage, respectively. θ_{fc} denotes the water content at field capacity, assumed to be the water content corresponding to a pressure head of −330 cm in a water column.

A.9 | Phosphorus

Regarding phosphorus, FLOWS simulates the behaviour of liquid-phase phosphorus (P_{liq}) based on decay reaction chains proposed by Mansell, Selim, and Fiskell (1977). Typically, inorganic phosphorus undergoes rapid conversion from orthophosphate to less soluble forms. Post application of inorganic P to soil, observed phosphorus soil solution concentrations are generally around 1 μg/cm^3 or lower (Mansell, Selim, and Fiskell 1977). The swift removal of phosphorus from the soil solution initially is often attributed to relatively fast reactions, such as physical adsorption to soil colloidal material. Phosphorus adsorption is commonly considered reversible (Van Der Zee and Van Riemsdijk 1986; Barrow, Madrid, and Posner 1981). Slower reactions involve the precipitation of phosphorus as AI, Fe and Ca phosphates. Additionally, a portion of the physically adsorbed phosphorus may gradually become occluded by matrices of Fe and AI components (chemisorption). Adsorption, precipitation and chemical immobilization mechanisms work concurrently and persistently over time to eliminate phosphorus from the soil solution.

The Mansell, Selim, and Fiskell (1977) approach, also implemented in FLOWS, assumes the transfer of phosphorus between solution, adsorbed, chemisorbed and precipitated phases to be governed by six reversible reactions. While adsorption occurs on pore walls and colloids, chemisorption (termed occlusion by Mansell, Selim, and Fiskell 1977) refers to the slow transformation of weaker physical bonds of adsorbed phosphorus into stronger chemical bonds. FLOWS assumes that adsorption follows an Nth-order kinetics (with an average N of 0.35, as suggested by Mansell, Selim, and Fiskell 1977) with a constant K_{ads1}, while all other reactions (desorption, chemisorption and mobilization, precipitation and dissolution) follow first-order kinetics with respective constants K_{ads2}, K_{chs1}, K_{chs2}, K_{prc1} and K_{prc2}, although higher orders can be accommodated in the code. Reaction rates are contingent on pH, the nature and content of clay minerals, organic matter, carbonates, cation saturation, and the amount of phosphate applied. Table A2 provides an overview of the equations governing the liquid-phase phosphorus transformation processes considered in FLOWS.

The remaining concentrations of P-PO_4 are transported through the soil by advection–dispersion:

TABLE A1 | The nitrogen transformation processes implemented in FLOWS. In the table, the Ss rates are in grammes per cubic centimetre of soil per day.

Process (reference)	Equation	Equation number
Nitrification (Cabon, Girard, and Ledoux 1991)	$Ss_{nit} = k_{nit} \times 1.07^{(T-T_{opt})} \frac{\theta}{\theta_{fc}} C_{NH} \quad \theta \le \theta_{fc}$ $Ss_{nit} = k_{nit} \times 1.07^{(T-T_{opt})} \frac{\theta_{fc}}{\theta} C_{NH} \quad \theta > \theta_{fc}$	(A14)
Denitrification (Lafolie 1991; McGechan and Wu 2001)	$Ss_{den} = 0 \quad \theta \le \theta_d$ $Ss_{den} = k_{den} \times 1.07^{(T-T_{opt})} \frac{\theta - \theta_d}{\theta_{fc} - \theta} C_{NO} \quad \theta_d \le \theta \le \theta_s \theta_d = 0.627\theta_{fc} - 0.0267 \frac{\theta_s - \theta}{\theta_s} \theta_{fc}$	(A15)
Root uptake of nitrogen	$S_{upNH} = K_{r,NH} S_r C_{NH}$ $S_{upNO} = K_{r,NO} S_r C_{NO}$	(A16)
Nitrogen losses to artificial drainage	$S_{drNH} = S_{dr} C_{NH}$ $S_{drNO} = S_{dr} C_{NO}$	(A17)

TABLE A2 | The phosphorus transformation processes implemented in FLOWS (Mansell, Selim, and Fiskell 1977). In the table, the *Ss* reaction rates are in grammes per cubic centimetre of soil per day.

Process	Equation	Equation number
Phosphorus adsorption	$Ss_{\text{ads}} = \frac{\partial(\rho_b C_{a,P})}{\partial t} = K_{\text{ads1}}\theta C_P^N - (K_{\text{ads2}} + K_{\text{chs1}})\rho_b C_{a,P} + K_{\text{chs2}} C_P$	(A18)
Phosphorus chemisorption	$Ss_{\text{chs}} = \frac{\partial(\rho_b C_{c,P})}{\partial t} = K_{\text{chs1}}\rho_b C_{a,P} - K_{\text{chs2}}\rho_b C_{c,P}$	(A19)
Phosphorus precipitation	$Ss_{\text{prc}} = \frac{\partial(\rho_b C_{p,P})}{\partial t} = K_{\text{prc1}}\theta C_P - K_{\text{prc2}}\rho_b C_{p,P}$	(A20)
Root uptake of phosphorus	$S_{\text{upP}} = K_{r,P} S_r C_P$	(A21)
Phosphorus losses to artificial drainage	$Ss_{\text{drP}} = S_{\text{dr}} C_P$	(A22)

$$\frac{\partial \theta C_P}{\partial t} = \frac{\partial q C_P}{\partial z} + \frac{\left(\partial \theta D \frac{\partial C_P}{\partial z}\right)}{\partial z} - Ss_P \tag{A25}$$

where S_{sP} represents the integrated contributions of adsorption, desorption, precipitation, dissolution, root uptake, drainage losses and fertilizer (both organic and inorganic) components:

$$\begin{aligned} Ss_P = &- Ss_{\text{minP}} - Ss_{\text{frtP}} - \theta\left(K_{\text{ads1}} C_P^N + K_{\text{prc1}} C_P\right) \\ &+ \rho_b\left(K_{\text{ads2}} C_{a,P} + K_{\text{prc2}} C_{p,P}\right) + Ss_{\text{upP}} + Ss_{\text{drP}} \end{aligned} \tag{A26}$$

In Equation (A26), as well as in the equations listed in Table A2, the subscript P denotes P-PO_4, while the subscripts a, p, and c represent the concentrations of adsorbed, precipitated, and chemisorbed phosphorus, respectively. Again, the source terms Ss_{minP} and Ss_{frtP} are derived by dividing the rates of mineralization and mineral phosphorus fertilizer addition (both measured in grammes per square centimetre of soil per day) by the incorporation depth, z_{fert}, to yield the corresponding *Ss* terms (expressed in grammes per cubic centimetre of soil per day), which are then added to each of the calculation nodes within z_{fert}.

Figure A3 summarizes the liquid-phase nitrogen and phosphorus transformations and transport simulation in FLOWS.

Appendix B

Detailed Description of the KWV Model

In KWV, the mean velocity, v (m/s), is calculated by Manning's equation:

$$v = \frac{S f^{\frac{1}{2}} R^{\frac{2}{3}}}{n} \tag{B1}$$

where n ($m^{1/3} s^{-1}$) is Manning's roughness coefficient and R is the hydraulic radius (area of flow divided by the wetted perimeter). Multiplying v by the flow cross-sectional area, A (m^2), provides the discharge Q (m^3/s).

As for solute transport, KWV integrates a 1D ADE to solve both the overland and channel mass transport. To be solved, the ADE requires the flow cross-sectional area, A, as well as the average velocity v for each calculation node, which may be obtained by firstly solving the kinematic wave equations for each simulation time step.

In this paper, for the application of the KWV model, the water coming to the runoff from the FLOWS simulations was routed according to the scheme given in Figure 1. Each of the different 0.5-ha field (200 m × 25 m) was considered as a planar overland flow element with water flowing to the downstream 200-m-long longitudinal ditch. A kinematic wave equation was applied to a unit-width strip of the field. Assuming the planar field with uniform soil profile and surface flow characteristics, the kinematic wave provides a distributed uniform water hydrograph, q_u(t) (L^3/LT), per unit length of the downstream draining ditch. Thus, these fluxes were considered as a distributed input to the kinematic wave equation to be applied for simulating routing along the ditch. Each ditch, in turn, provides a discharge Q_D(t) (L^3/T), which was considered as input for the kinematic wave applied to simulate the routing within the secondary drainage channel. The (previous) secondary channel also receives water fluxes directly from the shallow groundwater (the baseflow in Figure 1).

In any case, one should be aware that, even if this routing scheme is apparently simple from a macroscopic point of view, it represents in reality a quite complex system where the velocity may change drastically with respect to time and distance. Actually, crops in the field and spontaneous vegetation in ditches and channel, small-scale local changes in the topography and slope of the ditches and channels, continuously change direction and magnitudes of water fluxes. These local-scale heterogeneities frequently induce intermittent flow conditions, with water temporarily remaining at rest in the ditches and in the secondary channel, even for some days, and then mobilized again by a new runoff event. This induces travel times for the water (and solute) coming from runoff varying on a weekly (even monthly) time scale, as will be clearly demonstrated by looking at measurements in Section 3. In order to deal with such a complex (intermittent and nonuniform) and delayed runoff routing, by still assuming kinematic wave approximations, in this paper, we opted for a pragmatic adaption of Equation (B1) by using a very large Manning resistance parameter (much larger than those coming from the Manning coefficient tables) so as to catch the very delayed water and mass transport observed at the weir control sections.

Accordingly, Equation (B1) (in metres per day) becomes

$$v = \frac{S f^{\frac{1}{2}} R^{\frac{2}{3}}}{n_f} \tag{B2}$$

In this sense, the fictitious resistance parameter, n_f ($m^{1/3}\,day^{-1}$) in Equation (B2) should no longer be seen merely as a uniform flow resistance parameter, but rather as a fitting parameter accounting for the very delayed flow indicated by the observations, as well as for all the possible changes in nitrate mass not explicitly considered in the KWV model.

B.1 | Overland Flow

For overland flow, the following equation is used to calculate or specify (unit-length strip) discharge as a function of the mean depth of overland flow, y (m):

$$\begin{aligned} q_u &= \alpha y^m \\ \alpha &= \frac{1}{n}\sqrt{Sb} \\ m &= 5/3 \end{aligned} \tag{B3}$$

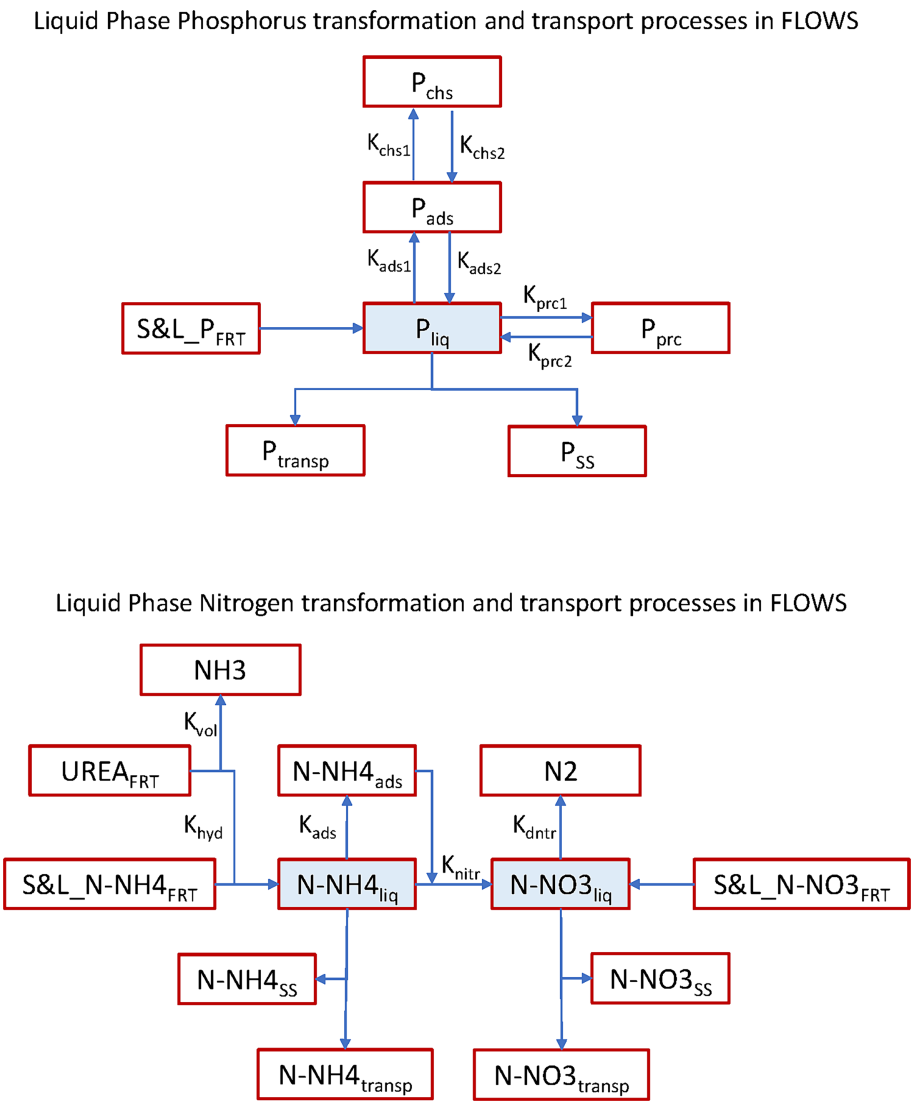

FIGURE A3 | Schematic view of the liquid nitrogen and phosphorus transformation processes.

where α and m are the routing parameters related to the overland surface and flow characteristics, n is Manning's resistance coefficient and Sb is the average slope of the overland flow element, having assumed that $Sb = Sf$.

Coupling Equation (B3) to the continuity equation gives

$$\frac{\partial y}{\partial t} + \frac{\partial q_u}{\partial x} = r_{ex} \tag{B4}$$

and using Equation (B3) for q_u provides the kinematic wave equation describing overland flow.

$$\frac{\partial y}{\partial t} + \alpha m y^{m-1} \frac{\partial y}{\partial x} = r_{\text{ex}} \tag{B5}$$

which can be solved to obtain y as a function of time, t, and horizontal distance from the inlet, x, as well as of the runoff water (L/T) calculated by FLOWS, that is, the excess water coming from rainfall and/or irrigation, r_{ex}, and induced by either Horton or Dunne mechanisms, as well as by lateral flow (artificial drainage). Thus, y can be used in Equation (B1) to obtain q_u. As mentioned, q_u will then be used as a distributed input for the channel flow in the ditches (input per metre of ditch).

B.2 | Channel Flow (for Ditches and Secondary Drainage Channel)

In this study, the cross section of ditches is assumed to be of semicircular shape whereas the secondary drainage channel cross section is trapezoidal. The equations for routing runoff by kinematic wave through ditches and secondary drainage channel are similar to those developed for shallow overland flow. Specifically, for ditches, Equation (B4) assumes the following shape:

$$\begin{gathered}\frac{\partial A}{\partial t} + \frac{\partial Q}{\partial x} = q_u \\ Q = \alpha A^m\end{gathered} \tag{B6}$$

where $Q(x, t)$ (L^3/T) is the ditch discharge and $A(x, t)$ (L^2) is the cross-sectional area of flow in the channel. The same equation applies for the secondary drainage channel, with q_u replaced by the discharge coming from a ditch. α and m have the same meaning as for the overland flow and must be defined for a particular channel cross-sectional shape, slope and roughness; thus, in general, they will differ among ditches, secondary drainage channel and overland flow.

KHW allows the user to change these parameters for each elemental field and ditch, as well as for each segment of the secondary drainage channel. The KWV code solves Equation (B5) for overland flow and

Equation (B6) for channel flow by using an explicit finite-difference numerical scheme.

B.3 | Solute Transport

KWV integrates a 1D ADE to solve the overland solute transport. The 1D for surface solute transport is as follows (Abbasi et al. 2003):

$$\frac{\partial(AC)}{\partial t} + \frac{\partial(AvC)}{\partial x} = \frac{\partial}{\partial x}\left(AD_{rn}\right)\frac{\partial C}{\partial x} + q_{\text{us}} \tag{B7}$$

where v (L/T) is the average flow velocity, C (M/L^3) is the solute concentration in the runoff and D_{rn} (L^2/T) is the dispersion coefficient in a given runoff flow cross section. The subscript rn means that the variable refers to the runoff water and may change with location x and with the section of the drainage network (elementary field, ditch or secondary drainage channel). The solute source–sink term, q_{us} (ML^{-1}T^{-1}), represents the solute fluxes coming from the field. It is obtained by multiplying $q_s(0,t)$ (ML^{-2}T^{-1}), which can be obtained from Equation (A10), by the area of the single field and then dividing it by the single field's width (WF in Table 3). Therefore, q_{us} can be calculated as follows:

$$q_{\text{us}} = q_s(0,t) \times LF \tag{B8}$$

where LF is the single field's length (Table 3).

In Equation (B7), D_{rn} at location x is obtained as follows:

$$D_{rn} = \lambda_{rn} v + D_{0,rn} \tag{B9}$$

where λ_{rn} (L) and $D_{0,rn}$ (L^2/T) are respectively the dispersivity and the molecular diffusion in free water.

As for Equations (B5) and (B6), Equation (B7) is also solved by an explicit finite-difference numerical scheme. Solving Equation (B7) requires the flow cross-sectional area A, as well as the average velocity V_{rn} for each calculation node i, which may be obtained by firstly solving the kinematic wave equations. Thus, V_{rn} may be calculated as $V_{rn,i} = Q_i/A_i$. This is why in KWV the kinematic wave equations (Equations B5 and B6) and Equation (B7) are solved sequentially at each time step.